UNIVERSITY OF ZULULAND

EFFECTS OF PARTICLES' SIZE AND COMPOSITION ON MAGNETIC PROPERTIES OF SUBSTITUTED FERRITE NANOPARTICLES

by

Prince Phathizwe Majozi

BSc, BSc (Hons) (UNIZULU)

Submitted in fulfilment of the academic requirements for the degree of Master of Science in the department of Physics and Engineering, University of Zululand.

Supervisor: Prof. J. Z. Msomi

Co-supervisor: Prof. T. P. Jili

February 2023

Acknowledgements

The success of this work has been achieved through the academic support from my supervisor, Prof. J.Z. Msomi to whom I would like to pass my gratitude. He has taught me essential concepts in condensed matter physics and improved my understanding of magnetic materials. He has also introduced me to various research facilities through networking, giving me new experiences from different institutions. I would like to thank my co-supervisor, Prof. T. P. Jili, for support and guidance. Lastly, I owe it to my mother and family to express sincere gratitude for their financial support and encouragement to carry on with my studies against all odds.

Dedication

This dissertation is dedicated to my late father Mr. C. M. Majozi, my mother Ms. E. A. T. Ngubane and my grandmother Mrs. A. Ngubane.

Declaration by candidate

I hereby declare that the work described in this dissertation was carried out by the candidate. This is the original work by the author and has not been in any form submitted to any institution or University. Credit has been given where the use of the work of others was made.

.....

P.P. Majozi

Abstract

This project presents the effects of particle size and composition on the magnetic properties of ferrites investigated by magnetization and electron spin resonance (ESR) spectroscopy. $Cu_xMn_{1-x}Fe_2O_4$, (Zn, Cd)$Fe_{1.2}Al_{0.8}O_4$, $Ni_xCo_{1-x}Fe_2O_4$ and $Cu_{0.5}Ni_{0.5}Fe_2O_4$ nanoferrites were produced by glycol-thermal reaction under a low reaction temperature of 200 °C. Structural properties were analysed by transmission electron microscopy (TEM) and X-ray diffraction (XRD).

For $Cu_xMn_{1-x}Fe_2O_4$, the majority of the XRD peaks were indexed to the cubic spinel phase. However, a small impurity peak at $2\theta \approx 52°$ attributed to α-Fe_2O_3 and Mn_2O_3 phases for samples $0.4 \leq x \leq 0.8$ was observed. The particle sizes varied between 8 nm and 16 nm. The particle size for the sample $x = 0.3$ ($Cu_{0.3}Mn_{0.7}O_4$), which did not show any impurity phases was about 8 nm. The reduction of lattice parameters as a function of increasing Cu content is attributed to the smaller Cu replacing Mn ions. Magnetization data revealed superparamagnetic $Cu_{0.3}Mn_{0.7}Fe_2O_4$ fine particles and spin-glass behaviour. Enhanced magnetization and coercive fields at 10 K were explained by the core-shell model and spin freezing.

An attempt to produce (Zn, Cd)$Fe_{1.2}Al_{0.8}O_4$ was made. The XRD spectrum of the Cd-based sample showed impurity phases. XRD analysis showed clean $ZnFe_{1.2}Al_{0.8}O_4$ with a particle size of about 6 nm. TEM images revealed nearly spherical particles with a reasonably narrow distribution of particle size which compared well with the value estimated from XRD data. ESR measurements showed a single-line signal indicative of dominant superexchange interactions. A small peak at very low magnetic field (about -500 $\leq H \leq$ 500 G) was observed for the Zn- based oxide annealed at 1000 °C. This anomalous peak may be due to the low field microwave absorption (LFMA) phenomenon that is not fully understood in magnetic materials.

$Ni_xCo_{1-x}Fe_2O_4$ were successfully indexed to the cubic spinel. An additional peak associated with α-Fe_2O_3 was observed for samples with $0.7 \leq x \leq 0.9$. XRD spectra revealed crystallite sizes ranging from 8 nm to 13 nm. There was no significant change in lattice parameters with increasing Ni concentration due to the small difference in their atomic radii. The ESR results showed single-line signals. Additional resonances

were observed at low fields which need further measurements. We suspect these additional resonance peaks to be due to LFMA. The Landé g-values varied between 1.98 and 3.6.

Nanosized $Cu_{0.5}Ni_{0.5}Fe_2O_4$ fine particles with particle sizes of about 12 nm were produced. XRD did not show any impurity phases. The as-prepared oxide was annealed from 500 °C to 1100 °C to investigate particle size effects. Grain growth to about 46 nm was observed after annealing at 900 °C. ESR data revealed enhanced magnetization on the sample annealed at 900 °C due to the large ferromagnetic domains.

Key words

Ferrites nanoparticles

Magnetization

Electron spin resonance

Contents

List of Figures

Chapter 1

Literature review

1.1 Introduction

Research on the magnetic nanomaterials has gained attention due to their technological and scientific importance [1, 2]. They have potential applications in magnetic resonance imaging (MRI), drug delivery, magnetic data storage, magnetic hyperthermia for cancer treatment, magneto-caloric refrigeration etc. [2–4].

Ferrites are a special group of magnetic materials with unusual optical, electrical and magnetic properties. They have applications in high density data storage, microwave absorption, high frequency transformer cores, MRI, electronic devices, electromagnets, magnetic hyperthermia for cancer treatment, frequency filters, sensors, tune generating circuitry of push button telephones, ferrofluids, magnetic drug delivery, microwave devices, catalytic and antibacterial agents [5–7].

The properties of ferrite compounds are dependent on the type, amount of constituent atoms, particle size, sample preparation method and the distribution of metal cations within the crystal lattice [8]. Doping effects and sample preparation methodology are important topics in ferrite research. Ferrites with fine particles have exceptional properties not observed in bulk materials [7, 9, 10]. These include phenomena such as superparamagnetism, spin-glass behaviour [11] and single-domain structure that transforms to multi-domain structure at a critical particle size [1, 12]. The unusual properties in nanoferrites are due to the distribution of atoms on the surface rather than in the core of the particles (large surface-to-volume ratio) [13–15]. A brief review of the crystal structure, synthesis and magnetic properties of ferrites is presented in the following sections.

1.2 Crystal structure

Ferrites have a crystal structure of a mineral spinel, $MgAl_2O_4$ [16, 17]. Mg ions are replaced by divalent metal ions such as Zn^{2+}, Co^{2+}, Cd^{2+}, Ni^{2+}, Mn^{2+} and Al ions

are replaced by Fe ions. Hence the general chemical formula of ferrites is $M\mathrm{Fe_2O_4}$, where M is a divalent metal ion [18]. In mixed ferrites M can be a mixture of metal ions.

The crystal structure of ferrites consists of tetrahedral (A) and octahedral (B) sites. Their chemical formula can also be expressed as $AB_2\mathrm{O_4}$ [19, 20]. Figure 1.1 **(a)** shows the unit cell of a spinel lattice. It is a closely packed face-centred cubic (FCC) structure of oxygen anions [20, 21]. The geometries of A- and B-sites are shown in Figure 1.1 **(b)**. The spinel lattice consists of 64 A- and 32 B-sites. There are 56 vacant A- and 16 empty B-sites. The presence of vacant sites in the spinel structure allows for the introduction of foreign atoms [22]. This has attracted many researchers on the doping effects in ferrite materials [23].

Ferrites are classified as either normal or inverse spinels depending on the distribution of metal ions. In normal spinels, divalent cations occupy tetrahedral sites and trivalent ions are in octahedral sites [24, 25]. Bulk $\mathrm{ZnFe_2O_4}$ is an example of normal spinel ferrites with all $\mathrm{Zn^{2+}}$ atoms occupying A-sites and $\mathrm{Fe^{3+}}$ ions at B-sites [24, 26]. For inverse spinel ferrites, the divalent cations are only found in B-sites and the trivalent ions are equally distributed between A- and B-sites [12, 24]. Cobalt ($\mathrm{CoFe_2O_4}$) and nickel ($\mathrm{NiFe_2O_4}$) ferrites are examples of inverse spinels with all $\mathrm{Co^{2+}}$ or $\mathrm{Ni^{2+}}$ ions at B-sites and $\mathrm{Fe^{3+}}$ ions equally distributed between A- and B-sites [12, 27].

The distribution of metal cations in ferrites can be expressed as [28]

$$(M^{2+}_{1-\lambda}\mathrm{Fe}^{3+}_{\lambda})_A[M^{2+}_{\lambda}\mathrm{Fe}^{3+}_{2-\lambda}]_B O^{2-}_4 \tag{1.1}$$

where λ is a parameter between zero and one representing the degree of inversion. Normal and inverse ferrites are ideal cases. Ferrite materials are partially inverse or normal [29].

For normal $ZnFe_2O_4$ (λ =0) and inverse $CoFe_2O_4$ (λ = 1), equation 1.1 becomes [32, 33].

$$(Zn^{2+})_A[Fe_2^{3+}]_BO_4^{2-} \tag{1.2}$$

and

$$(Fe^{3+})_A[Co^{2+}Fe^{3+}]_BO_4^{2-} \tag{1.3}$$

for Zn- and Co-ferrites.

Cobalt ferrites have remarkable physical properties such as high coercive fields, high magneto-crystalline anisotropy constant, moderate saturation magnetization, good mechanical hardness and chemical stability [27]. These properties make them suitable for applications in electronics, magnetic recording, magnetic fluids, magnetic drug delivery, sensors, high quality filters, phase filters, optoelectronics, photo-catalytic activity, spintronics and transformer cores [2, 18]. Cobalt ferrite nanoparticles also have applications in hyperthermia and genetics, for their suitability in isolation and purification genomic deoxyribonucleic acid (DNA) [34]. Zinc ferrites are impressive compounds and have been used in MRI, photocatalysis, anti-cancer drug sensors, hyperthermia and gas sensing [12, 13, 35]. The properties of mixed $Zn_{0.5}Co_{0.5}Fe_2O_4$ are different from those of pure $ZnFe_2O_4$ and $CoFe_2O_4$.

1.3 Magnetic properties

The magnetic properties of ferrites are due to superexchange interactions, where the magnetic moments interact through intervening oxygen ions [27]. MnO is the simplest example of a compound with superexchange interactions. The electron spin orientation of one Mn ion induces an opposite spin on another Mn ion through the non-magnetic oxygen ion as shown in Figure 1.2. This results in an antiferromagnetic alignment of Mn atoms.

The magnetic interactions in ferrites are characterized by intrasublattice (A-O-A and B-O-B) and intersublattice (A-O-B) exchange integrals. The magnetic spins at A- sites interact through A-O-A while those at B-sites interact trough and B-O-B intrasublattice exchange integrals. Superexchange interactions are negative i.e., they tend to align magnetic moments antiparallel [6, 8]. The A- and B-site magnetic

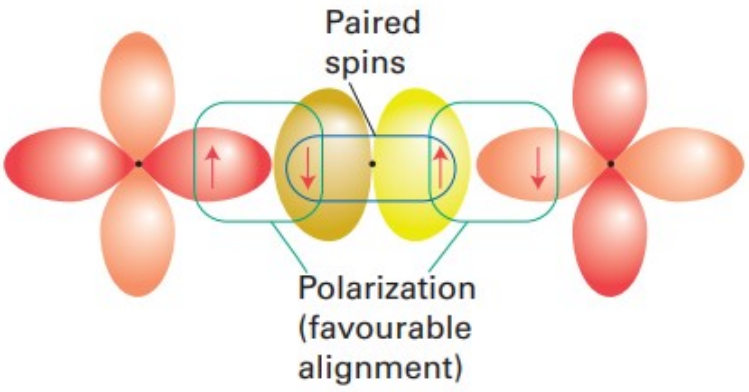

Figure 1.2: Superexchange interaction [41].

moments interact through A-O-B exchange integrals.

Substitution of foreign atoms can modify the magnetic properties [22]. Dilution by non-magnetic ions in a spinel structure can result in broken exchange paths and thus reduced magnetization [36]. Substitution by magnetic atoms can enhance magnetization [37, 38].

Magnetism in ferrites is ferrimagnetism, where unequal magnetic moments are antiparallel to each other. The magnetization in A- (M_A) and B-sites (M_B) are due to unequal magnetic moments. The resultant magnetization in ferrite compounds is $M = \mid M_A - M_B \mid$ and depends on the constituent atoms [27, 39]. In a normal spinel $ZnFe_2O_4$, non-magnetic Zn^{2+} ions contribute zero magnetization at A-site (M_A) and antiparallel magnetic moments of Fe^{3+} ions at B-site also give rise to $M_B = 0$ [27, 40]. In inverse $CoFe_2O_4$, equal amounts of antiparallel Fe^{3+} ions at A- and B-site result to zero net magnetization [2]. The magnetization is thus due to Co^{2+} magnetic spins at B-sites.

The dependence of the magnetic properties of ferrites on composition and sample preparation method has resulted in several articles appearing in the literature associated with doping effects and synthesis methods [1, 19, 29, 32, 35, 39, 42–59]. Cd-doped $NiFe_2O_4$ ($Cd_xNi_{1-x}Fe_2O_4$) showed an increase in lattice parameter with increasing Cd concentration. Maximum saturation magnetization was observed for $x = 0.3$. This was reduced with the further addition of Cd-ions [56]. Cr substituted $NiFe_2O_4$ oxides ($NiCr_xFe_{2-x}O_4$) showed lower saturation magnetization attributed to a lower magnetic moment of Cr^{3+} (3 μ_B) compared to Fe^{3+} (5 μ_B) ions [32]. A

study of $Ni_{0.2}Mg_{0.8}Fe_2O_4$ ferrites revealed a high dielectric constant and low coercive magnetic field, making them promising candidates for supercapacitors and magnetic recording [50].

Rare earth substitution has interesting effects on magnetic properties of ferrites due to the occupancy of their 4f-shells [27]. Gadolinium (Gd) substitution in magnesium ferrites ($MgGd_xFe_{2-x}O_4$) was observed to improve resistivity, initial permeability and saturation magnetization [49]. Substitution of Fe^{3+} (5 μ_B) by Gd^{3+} (8μ_B) resulted to high saturation magnetization and increased remanence magnetization [60]. Mössbauer studies on these ferrites also showed ferromagnetic behaviour. The reduced magnetization in Sm-based oxides observed was explained by less magnetic Sm^{3+} ion concentration. Due to the low dielectric loss factor and high resistivity of Sm-Mg ferrites, they are potential candidates for high frequency applications [60].

Low coercivity in magnetic materials is a characteristic for soft magnetic behaviour [55, 61], which is important in transformer cores and telecommunication applications [36]. Aluminium doping has been practised due to the softening effects observed in Aluminium doped ferrites [14, 36, 55, 62, 63]. Samad Zare et al. [62] prepared $Co_{1-x}Zn_xFe_{2-x}Al_xO_4$ using a co-precipitation technique. They reported a softening effect due to non-magnetic Al and Zn substitution. Saturation magnetization initially increased from $x = 0.0$ to $x = 0.4$ and decreased with a further increase of x, which is due to strengthening of A-O-B super-exchange interaction and increase in spin canting, respectively. Aluminium in $Zn_xCo_{1-x}Fe_{2-x}Al_xO_4$ synthesized by glycol-thermal technique [36] displayed a similar softening effect. A brief discussion on the synthesis of ferrites is given below.

1.4 Synthesis

Bulk spinel ferrites can be prepared by using solid state reaction from high-purity metal oxides [18, 28, 29, 32–35, 56, 64]. The process involves annealing twice at high temperatures (between 800 °C and 1400 °C). This technique is sometimes called a double sintering ceramic technique or standard ceramic process [8]. The starting oxides can be mixed by hand grinding or high energy ball milling. Solid state reaction

has been successful in the production of good quality ferrites and improved properties with grain sizes of about 100 nm [60]. High sintering temperatures and the mixing of oxides can be a disadvantage of this technique. Some materials may show low quality when produced at high sintering temperatures due to the melting of some atoms. This can result in the loss of stoichiometry of the desired compounds. Non-homogeneous shape and particle size distribution can also be observed in compounds produced by this technique and the risk of contamination is high [29, 56].

Different synthesis techniques for ferrite nanoparticles such as sol-gel [3,4,39,51,65], co-precipitation [2,6,7,27,53], sol-gel auto combustion [32], microwave assisted hydrothermal [65], hydrothermal [48, 66], micro-emulsion [67, 68], solvothermal [20], microwave irradiation-assisted technique [40], solution combustion [43], auto-combustion [69, 70], citrate precursor [44, 71, 72], self-combustion [73, 74], phase transformation [75], mechanochemical processing [58], citrate-precursor auto-combustion [76], thermal treatment [13, 72], microwave combustion [77], polymer pyrolysis [18], spray pyrolysis [70], electrodeposition [78], normal micelles [34] and reverse micelles [34] have appeared in literature for the synthesis of nanoferrites.

With the development of nanotechnology, synthesis methods for ferrites with fine particles are being developed. The bulk counterparts can be produced from the as-prepared nanoparticles through annealing processes [14]. The focus of the current work is on the magnetic properties of nanocrystalline compounds with the chemical formulae $Cu_xM_{1-x}Fe_2O_4$ (M = Mn, Ni), $Ni_xCo_{1-x}Fe_2O_4$, and (Cd, Zn)$Al_{0.8}Fe_{1.2}O_4$ synthesized by glycol-thermal method.

Glycol-thermal reaction is able to produce materials under low reaction temperature. Annealing is not required to produce the as prepared samples.

1.5 Problem statement

The magnetic properties of ferrite materials are dependent on the composition, particle size and sample preparation method. The random distribution of metal cations also affects the properties and is dependent on the sample preparation technique.

Samples from different laboratories can show different ferrite properties which can be tuned for applications by controlling the particle size and composition.

Furthermore, the novel LFMA phenomenon is not fully understood in magnetic materials [79, 80]. Materials with this phenomenon need very low (non-resonance) applied magnetic fields [80]. Hence they have potential applications in low field magnetic sensors, field-controlled microwave absorbers, junction tunneling, spin valves etc. [79, 82].

Any systematic study of the magnetic properties of ferrite materials is important since they have a wide range of applications in the electronic industry and medicine. In this project, the magnetic properties of bulk and nanostructured ferrite materials have been studied by magnetization and ESR measurements.

1.6 Aims and Objectives

The aim of this project is to investigate the effects of composition and particle size on the magnetic properties of substituted mixed ferrites and search for LFMA phenomenon.

The objectives are thus to produce bulk and nanoferrites and characterize them by using XRD, TEM, magnetization and ESR measurements. In this attempt $Cu_xMn_{1-x}Fe_2O_4$, (Zn, Cd)$Fe_{1.2}Al_{0.8}O_4$, $Ni_xCo_{1-x}Fe_2O_4$ and $Cu_{0.5}Ni_{0.5}Fe_2O_4$ will be synthesized by glycol-thermal reaction.

1.7 Structure of the dissertation

The magnetic properties of the compounds studied are presented in Chapter 2. Experimental details are given in Chapter 3. The results are presented in Chapters 4 to 7. Conclusions and future studies are given in Chapter 8.

If the angular speed of an electron is ω,

$$I = -\frac{e}{T} = -ef = -\frac{e\omega}{2\pi}, \tag{2.3}$$

hence

$$\mu = IA = -\frac{1}{2}e\omega r^2 = -\frac{eL}{2m_e}. \tag{2.4}$$

The orbital magnetic moment is proportional to the angular momentum (L). L is quantized in the units of $\hbar$, i.e. $L_z = m_l\hbar$. This gives

$$\mu_z = -\left(\frac{e\hbar}{2m_e}\right) m_l = -\mu_{\mathrm{B}} m_l, \tag{2.5}$$

where $\mu_{\mathrm{B}} = 9.2732 \times 10^{-24}$ J/T and is the lowest value of magnetic moment called the Bohr magneton. The number m_l is the orbital magnetic quantum number. Taking into account the electron spin, the total angular momentum $\vec{J} = \vec{L} + \vec{S}$ and the corresponding magnetic moment is $\mu = \gamma J$, where γ is called the gyro-magnetic ratio [84, 85]. For pure orbital motion ($S = 0$)

$$\gamma = -\frac{e}{2m_e}. \tag{2.6}$$

For pure spin ($L = 0$)

$$\gamma = -\frac{e}{m_e}. \tag{2.7}$$

The magnetic moment of an atom is due to both electron orbital and spin motion and is proportional to the total angular momentum J, i.e.

$$\mu \propto J. \tag{2.8}$$

2.1 Magnetic moment of an atom

The magnetic moment of an atom is determined by the contributions of all the electrons [86, 87]. The angular momenta of its electrons couple to give a total angular momentum J. The interaction between the angular momentum of one electron and the spin angular momentum of another or the same electron is called the spin-orbit coupling. Orbit-orbit interaction exists between the orbital angular momenta of different electrons. The angular momentum of one electron has stronger interaction with its own spin than with those of the other electrons. Experiments show a preference for orbit-orbit and spin-spin interactions. This results to the coupling

referred to as Russell-Sounders (L-S) coupling [84, 87], discussed below.

In this scheme, spin-spin interactions give rise to a total resultant spin:

$$\vec{S} = \sum \vec{s_i}. \tag{2.9}$$

Orbit-orbit interactions give rise to the total angular momentum:

$$\vec{L} = \sum \vec{l_i}. \tag{2.10}$$

The resultant of $\vec{L}$ and $\vec{S}$ couple through spin-orbit interactions to form the total angular momentum $\vec{J}$.

L-S coupling works properly for most of the elements. The ground state configurations of magnetic moments can be deduced using Russel-Sounders coupling and Hund's rules [87]. The resulting total magnetic moment of an atom is related to J as:

$$\mu_{tot} = \frac{e\hbar}{2m_e}\sqrt{J(J+1)} = g\mu_{\mathrm{B}}\sqrt{J(J+1)}, \tag{2.11}$$

where g is a dimensionless Landé g-factor given by:

$$g = 1 + \frac{J(J+1) + S(S+1) - L(L+1)}{2J(J+1)}. \tag{2.12}$$

The value of $g = 2$ when there's no contribution of orbital motion to the net magnetic moment and $g = 1$ whenever electron spins sum up to zero [88]. There are different types of magnetism in solid materials, namely, diamagnetism, ferro-, antiferro- and ferrimagnetism as presented in the sections below.

2.2 Diamagnetism

Diamagnetism is a weak non-permanent type of magnetism that is characterized by negative susceptibility [86]. It is observed in molecules with closed shells such as noble gases, diatomic gases and covalent solids [88]. When an external magnetic field is applied to such materials, a very small magnetic field is induced in the opposite direction of the external field [86].

2.3 Paramagnetism

Figure 2.2 shows the arrangement of magnetic moments for various magnetic materials. The magnetic moments of paramagnetic materials are randomly oriented as shown in Figure 2.2 (a). The magnetic moments are aligned parallel to each other in ferromagnetic materials as shown in Figure 2.2 (b). Figure 2.2 (c) and (d) show the antiparallel alignment of magnetic moments for antiferromagnetic and ferrimagnetic materials, respectively. In antiferromagnetic materials, equal magnetic moments are aligned in an anti-parallel manner. On the other hand, ferrimagnetic materials exhibit anti-parallel alignment of unequal magnetic moments. Ferro-, antiferro- and ferrimagnetism will be further discussed in the following sections.

In the presence of an external magnetic field, the magnetic moments of a paramagnet become aligned with the direction of the magnetic field resulting to a net magnetic moment. Paramagnetism occurs in paramagnets with unpaired electrons. Chlorides, sulphates, carbonates of manganese, chromium, iron, cobalt, etc. are examples of paramagnets [89]. According to the Curie law, susceptibility in paramagnets varies with the temperature as [88]:

$$\chi = \frac{C}{T}, \tag{2.13}$$

where C is a Curie constant. The magnetic susceptibility of materials according to this law varies with temperature as shown in Figure 2.3 (a). Curie law is based on the assumption that there are no interactions between atoms or molecules. It fails on most materials. Curie-Weiss law is given by the equation [88]:

$$\chi = \frac{C}{T - \theta_p}. \tag{2.14}$$

This accounts for the interatomic interactions and compares well with the experimental results. θ_p is the paramagnetic Curie point. According to the mean-field theory, there is an internal magnetic field (called molecular field H_m) proportional to the magnetization of a material

$$H_m = \gamma M. \tag{2.15}$$

It can be shown that the parameter $\theta_p = \rho C \gamma$, where ρ is the density of a material and γ is the molecular field constant.

At temperatures close to the Curie point, theoretical predictions by equation (2.21) deviate from experimental values. As a result, there is a slightly different value of the experimental Curie temperature $\theta_f < \theta_p$ is observed called a ferrimagnetic Curie point. This is because of short-range magnetic order (spin-clusters) at temperatures slightly above T_c [97, 98].

Chapter 3

Experimental details

3.1 Introduction

The dependence of the magnetic properties of ferrite materials on chemical composition and particle size has attracted many researchers. The properties are also influenced by the random distribution of atoms involved among the interstitial sites. Some atoms have a preference for tetrahedral (A) or octahedral (B) sites. The distribution of metal cations, which affects the properties is also dependent on the sample preparation technique and particle size. In this work about 1 g nano-sized ferrites with chemical compositions $Cu_xMn_xFe_{1-x}O_4$ ($0 \leq x \leq 0.8$), $Ni_{0.5}Cu_{0.5}O_4$, $Ni_xCo_{1-x}Fe_2O_4$ ($0 \leq x \leq 1$), $CdAl_{0.8}Fe_{1.2}O_4$ and $ZnAl_{0.8}Fe_{1.2}O_4$ were produced by glycol-thermal reaction and analysed by using XRD, ESR and magnetization measurements.

3.2 Synthesis of materials

The as-prepared fine powdered ferrite compounds studied in this work were synthesized by a technique referred to as glycol-thermal reaction. The stoichiometric amounts of $Ni(NO_3)_2{\cdot}6H_2O$ (99.999 %), $Co(NO_3)_2{\cdot}6H_2O$ (99.999 %), $FeCl_3{\cdot}6H_2O$ (99.999%) and $ZnCl_2{\cdot}6H_2O$ (hexahydrate) supplied by Aldrich were used as starting materials. The steps followed in this sample preparation method are shown in Figure 3.1. The chlorides and nitrates were weighed and mixed thoroughly in deionized water using magnetic stirrer for about 15 minutes.

A 5 M solution of NaOH was then drop-wisely added to the mixture during rapid stirring while monitoring pH between 9 and 10. This was done to ensure full precipitation. The precipitate was then repeatedly washed with deionized water to get rid of chloride ions.

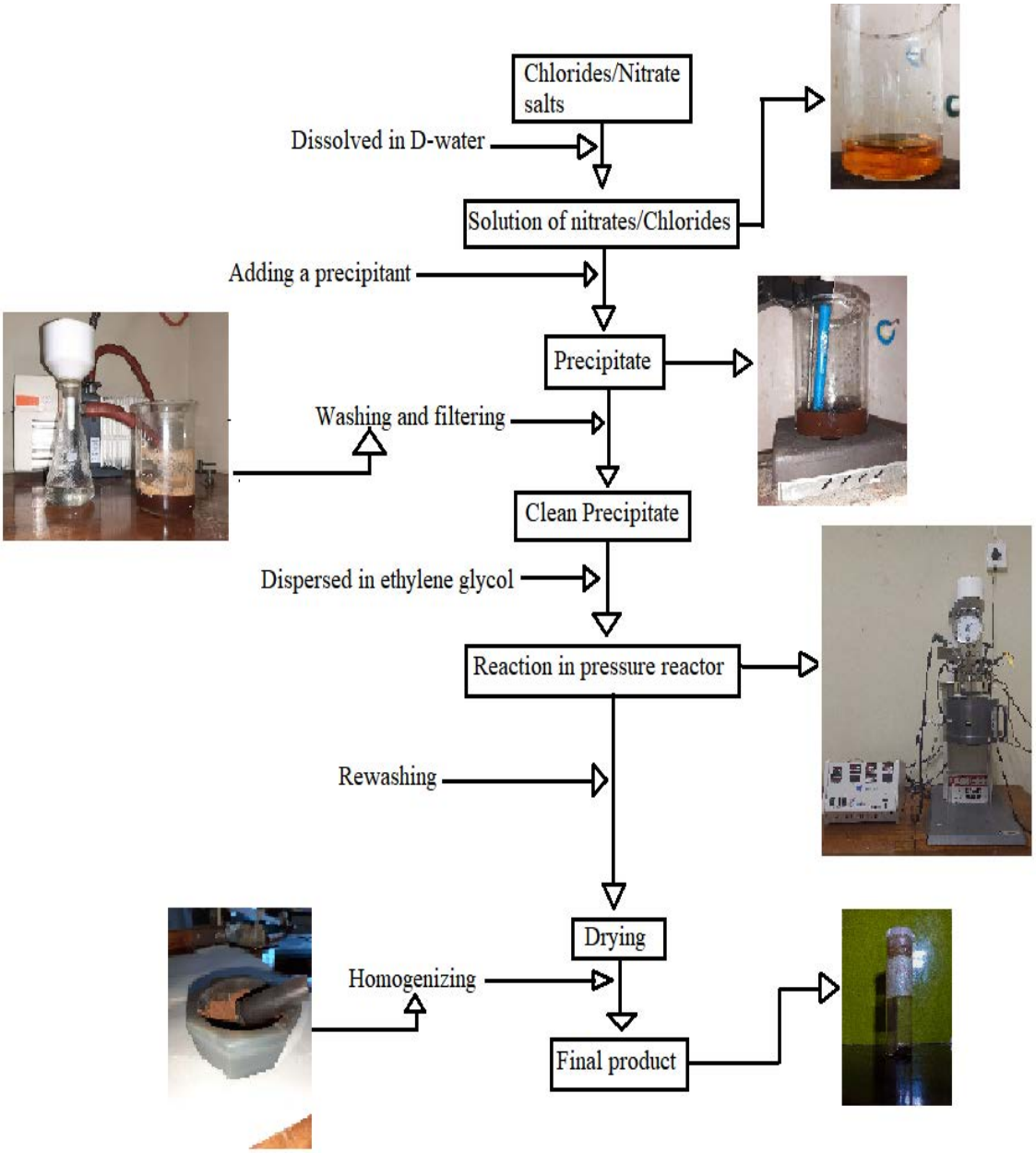

Figure 3.1: Glycol-thermal technique flow diagram.

During the washing process, deionized water was filtered through Whatman GFF glass microfibre filter papers, using a Büchner funnel and 2 L filtration flask as shown in Figure 3.1. The clean precipitate was dispersed in ethylene-glycol and placed in a 1000 mL Model 4848B Parr stirred general purpose pressure reactor shown. Ethylene glycol has an advantage of higher reaction temperature of 200 °C. The temperature was set to 200 °C and pressure was allowed to increase to about 380 kPa. These conditions were kept for 5 hours while stirring at about 31.4 rad/s.

The cooled product was rewashed and dried in a microwave oven at 80 °C overnight to remove excess moisture. After homogenization by agate mortar and pestle, the synthesized samples were taken for X-ray diffraction measurements to confirm the quality of compounds produced before further characterizations.

3.3 X-ray Diffraction (XRD)

XRD is a very powerful and non-destructive technique that uses monochromatic X-rays to determine the structural properties of crystalline materials [45, 99]. M. Laue, W. Friedrich and P. Knipping were involved in the discovery of this technique for crystals in 1912, which was further developed by W. H. Bragg and his son W. L. Bragg [99]. An X-ray tube is shown in Figure 3.3. The major parts are cathode, anode and glass envelope, supporting anode and cathode. X-rays are produced within the X-ray tube when the accelerated electrons from the filament (cathode) strike the atoms of the target (anode). Both characteristic and Bremsstrahlung X-rays are produced.

During the X-ray diffraction experiment, monochromatic radiation from the X-ray tube hit the surface of the specimen under investigation as shown in Figure 3.4. X-rays are reflected off successive layers of atoms. Constructive interference of reflected rays occurs when the optimal path difference $= n\lambda$ where n is an integer. That is, X-rays interfere constructively when [99, 102]

$$2d \sin\theta = n\lambda. \tag{3.1}$$

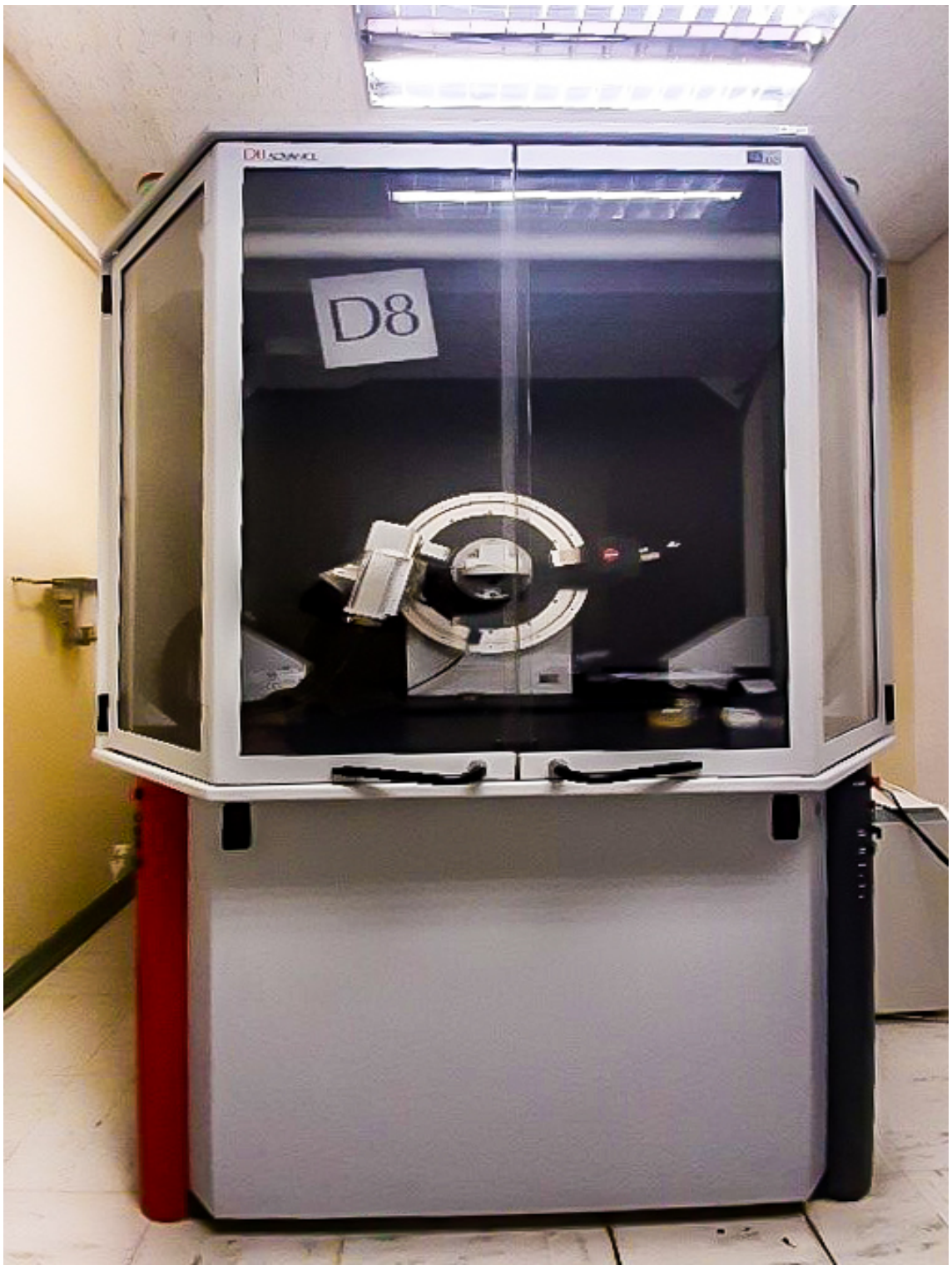

Figure 3.5: X-ray diffractometer (D8 Advanced) (UNIZULU).

where a, b and c are the lattice parameters. For cubic crystals ($a = b = c$), d is related to the size of a unit cell a as [2, 103]

$$d = \frac{na}{\sqrt{h^2 + k^2 + l^2}}. \tag{3.3}$$

In this particular work, a D8 Advanced X-ray diffractometer shown in Figure 3.5 was used for XRD analysis.

3.4 Transmission electron microscopy (TEM)

TEM is a technique that uses transmitted electrons to provide morphological properties of specimen. In this particular work, the FEI Tecnai Field Emission Microscope (G2 F20 X-Twin MAT, Eindhoven) shown in Figure 3.6 was used for TEM analysis.

Before the TEM measurements were carried out, the fine-powdered samples were prepared. During the preparation process, small grains of the powdered samples were placed in vials, dissolved with ethanol and sonicated for about 20 minutes to ensure even dispersion of the particles. Solutions of the specimens were drop-wisely deposited to separate TEM copper grid meshes. The specimens were dried using a desk lamp for about 10 minutes. The support grids with specimens were carefully placed in the sample holder using tweezers. One specimen at a time was loaded into the TEM machine using the sample holder.

When the filament is turned on, a high energy (100-400) keV electron beam is accelerated from the electron gun and focused on the sample using electromagnetic lenses. Some of the electrons are transmitted while others are absorbed or scattered by the sample. The transmitted electron beam is then projected on a fluorescent screen forming an image showing the morphology of the sample. This image can be magnified up to about 10^6 times [104, 105]. Shown in Figure 3.7 is the TEM cross-sectional diagram with components of the TEM machine.

Figure 3.6: Transmission electron microscope (UCT).

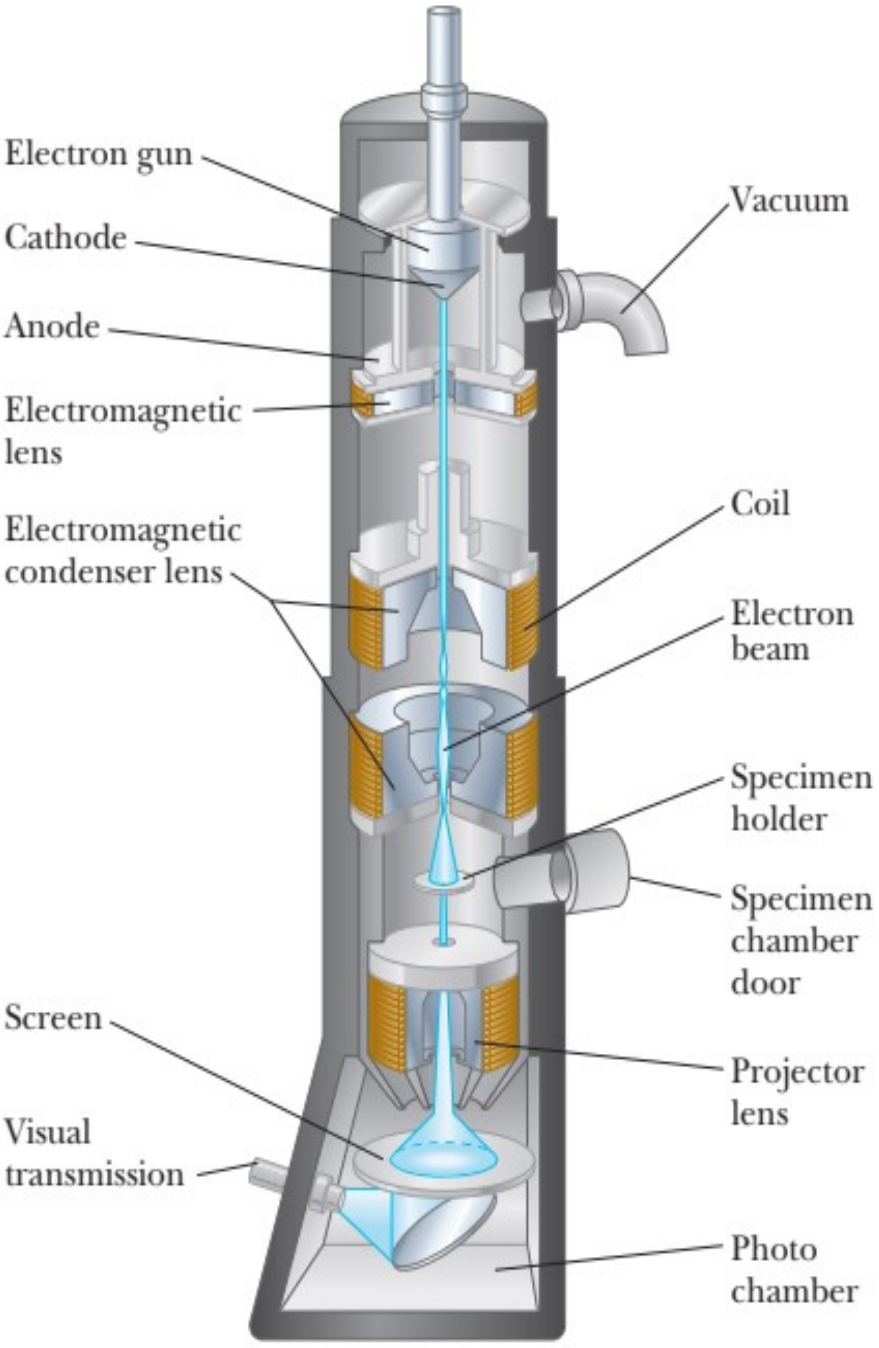

Figure 3.7: TEM cross sectional diagram [106].

3.5 Magnetization measurements

Magnetization is the magnetic moment per unit volume, i.e., [92, 107]

$$\vec{M} = \frac{\vec{\mu}}{V} = \frac{1}{V}\sum_i \vec{\mu_i}. \tag{3.4}$$

It is proportional to the magnetic field strength i.e. $\vec{M} = \chi\vec{H}$, where χ is the susceptibility of the material. By examination of χ, one can deduce the type of magnetism in a material [108]. Since the volume varies with temperature, it is convenient to express magnetization in terms of mass by using the quantity $\vec{\sigma}$ called specific magnetization defined as

$$\vec{\sigma} = \frac{\vec{\mu}}{mass} = \frac{\vec{\mu}}{\rho V} = \frac{\vec{M}}{\rho}, \tag{3.5}$$

where ρ is the density of a material [109].

Magnetization gives information on the ordering of magnetic moments in response to the applied or internal magnetic fields. The magnetic order of spins is also dependent on temperature. Para-, ferro-, antiferro- and ferrimagnetic materials have characteristic magnetic transition temperatures. In the current work magnetization measurements were done at certain temperatures (isothermal) and as a function of temperature under the influence of magnetic field.

A Superconducting Quantum Interference Device (SQUID) is a magnetization measurement device made up of a superconducting loop separated by Josephson weak links. It consists of a superconducting magnet (solenoid) that requires cooling with liquid helium or nitrogen to keep it at low temperatures to maintain its superconducting property. Both the sample chamber and a detector need to be cooled with liquid helium and or nitrogen. It is a preferred device due to its properties like high sensitivity, easy calibration, linear response to magnetic flux and a sufficiently small interaction with samples [110]. SQUID offers an automated magnetization measurement at various temperatures as a function of external magnetic field [47]. A SQUID magnetometer of Quantum Design model was used in this work.

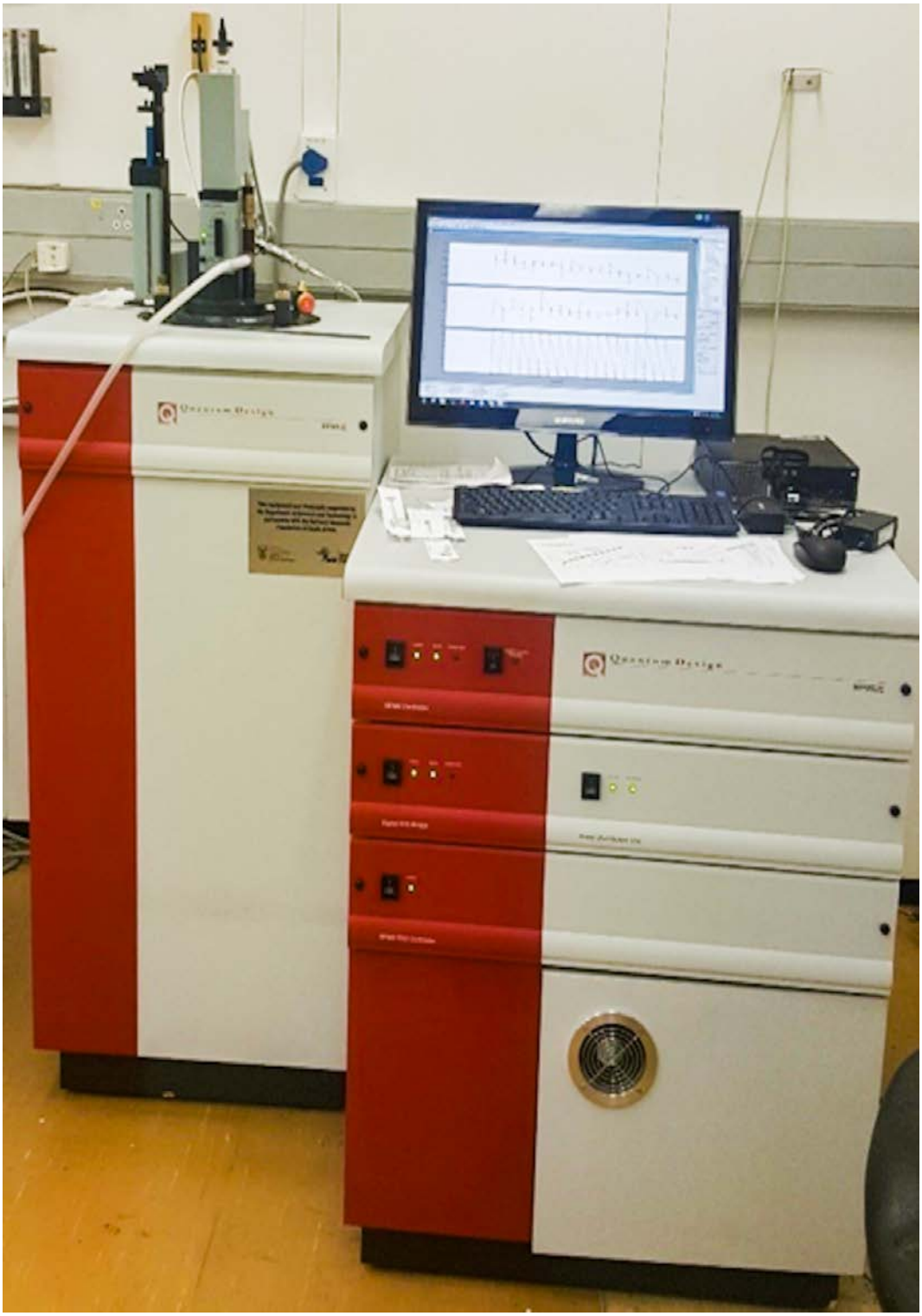

Figure 3.8: SQUID magnetometer (Quantum Design) used in this work (UKZN).

In principle, the empty sample holder had to be measured for the elimination of the background signal. About 0.02 g of the specimen was weighed and inserted into the sample holder.

The mounting station was used to ensure the correct positioning of the sample. The specimen holder was mounted on the rod for insertion into the SQUID device. Computer software was used to install and centre the sample using an auto-tracking function. The specimen details like mass, name and dimensions were specified in the measurement data. After the specifications of temperature, magnetic field and other parameters, the magnetization measurements could be performed.

3.6 Electron spin resonance (ESR)

ESR spectroscopy is an important tool to study the magnetic properties of materials. Atoms have discrete states with different energies. Measurements of energy differences (ΔE) between atomic or molecular states give information on the structure and electron dynamics of the sample under investigation [36]. The relation between ΔE and the electromagnetic radiation given by Plank's law allows for the measurement of ΔE. Electromagnetic radiation is absorbed when $\Delta E = h\nu = g\mu_B B_0$, where $h =$ Plank's constant, $B_0 =$ magnetic field and ν is the radiation frequency [111].

The ESR signal intensity is also proportional to the magnetization of the sample. When there is a large anisotropy magnetic field $H = 4\pi M_s$ (where M_s is the saturation magnetization), each grain resonates independently. The ESR curve is a broad envelope of grain resonances [112]. If the anisotropy field is small for saturation magnetization, linewidths of the signal are proportional to the porosity (p), i.e. $\Delta H = 1.5 M_s p$.

During the ESR experiment, the specimen is irradiated with microwaves at a constant frequency in the order of 10^{10} Hz [45, 113] and the signal is recorded while scanning the magnetic field in the region of interest. During spectroscopic measurements like NMR, frequency is varied and absorption peaks in the spectrum correspond to energy differences of the atomic or molecular states shown in Figure 3.9. In the case of ESR, ν is kept constant and the signal is recorded as a function of B_0.

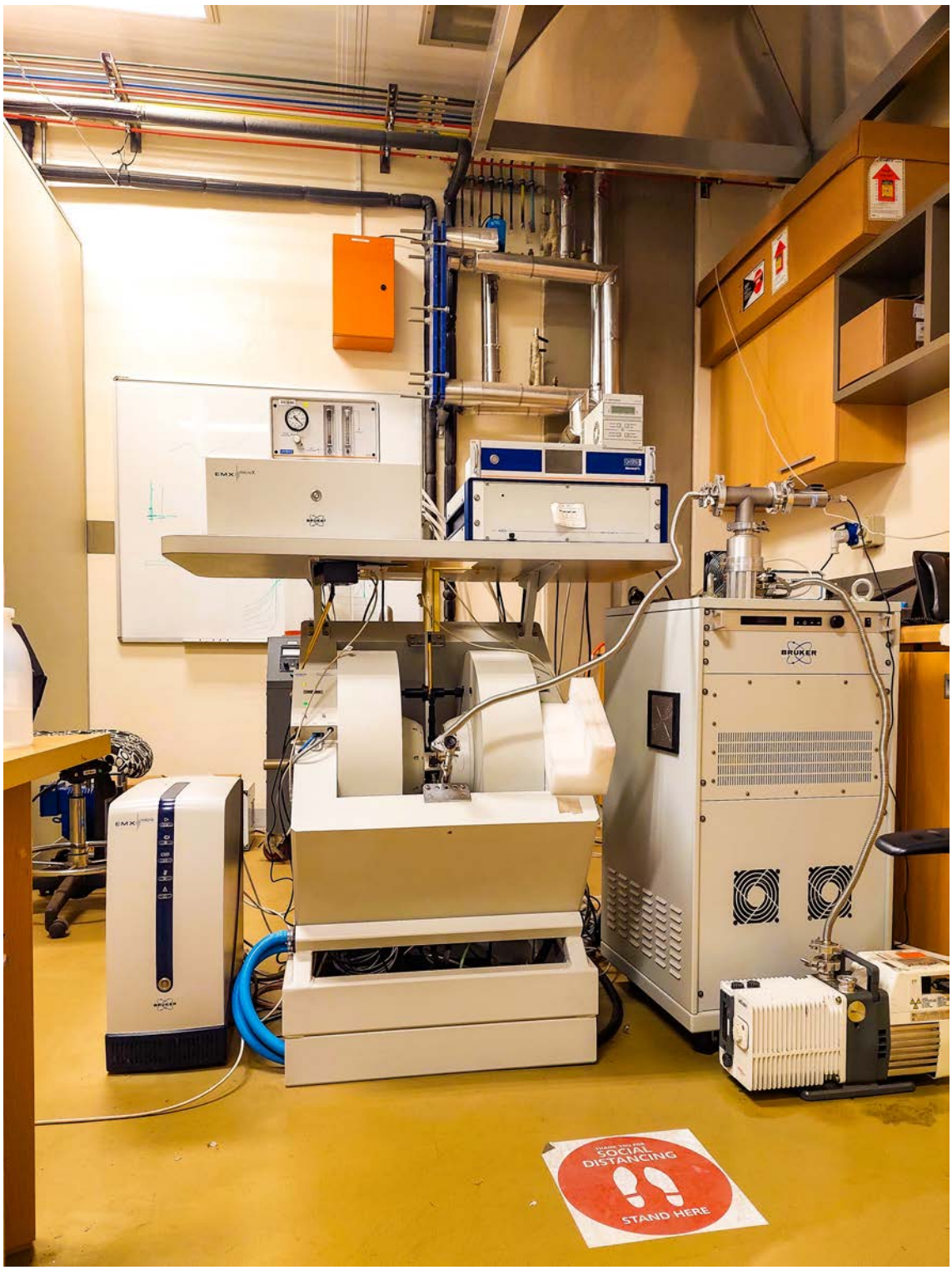

Figure 3.10: Bruker ESR spectrometer (UNISA).

Chapter 4

Magnetic properties of $Cu_xMn_{1-x}Fe_2O_4$ fine powders

4.1 Introduction

Manganese ferrites are known as soft magnetic materials owing to their high magnetic permeability and low dielectric losses [115, 116]. The remarkable properties of $MnFe_2O_4$ nanoferrites make them suitable candidates for technologies like microwave devices, computer memory chips, transformer cores, rod antennas, catalysis, recording media and other telecommunication applications [115, 116].

Doping manganese ferrites with copper ions can modify their structural, magnetic and electrical properties for various applications. Substitution of manganese ions by smaller copper ions can cause lattice parameter contraction and lattice distortion [115, 117, 118]. The incorporation of copper ions in $MnFe_2O_4$ can also enhance electrical conductivity as a result of reduced hopping lengths [115].

S. Meena et al. [116] reported an enhancement of the photocatalytic activity of 90 % under 20-minute sunlight irradiation upon substitution of Mn by Cu ions. S. Yuvaraj et al. [118] studied the electrical properties of Cu-Mn oxides synthesized by chemical co-precipitation. They reported the ferromagnetic nature of these ferrites and a decrease in optical band gap from 1.83 to 1.51 eV. An increase in electric conductivity on $Cu_xMn_{1-x}Fe_2O_4$ with the increase in copper concentration produced by co-precipitation was reported by L. M. Salah et al [115]. In this chapter the magnetic properties of $Cu_xMn_{1-x}Fe_2O_4$ ($0 \leq x \leq 0.8$) oxides prepared by glycol-thermal method and characterized by using XRD and magnetization measurements are presented.

4.2 Results and Discussions

4.2.1 X-Ray diffraction results

Figure 4.1 shows the XRD patterns for $Cu_xMn_{1-x}Fe_2O_4$ ($0 \leq x \leq 0.8$) compounds investigated. The major peaks (220), (311), (400), (422), (511) and (440) for both doped and undoped compounds are indicative of cubic spinel phase [9,119–121]. The XRD pattern for an undoped sample was shifted to the right because a different XRD source (Co-Kα) was used for undoped sample. Small impurity peaks at $2\theta \approx 29^\circ$ and 52° indicated by an asterisk (*) may be due to α-Fe_2O_3 and Mn_2O_3 phases [9,122,123]. Similar impurity phases were reported in $Mn_xZn_{1-x}Fe_2O_4$ oxides prepared by sol-gel auto combustion technique [32]. The presence of α-Fe_2O_3 was also reported by M. Rezaei [124] in sol-gel hydrothermally prepared $MnFe_2O_4$ which disappeared with the addition of polyvinyl alcohol (PVA) during sample preparation. The crystallite sizes (D_s) were calculated by using the Debye-Scherrer formula, following standard practice [22, 24, 120]:

$$D_s = \frac{0.91\lambda}{\beta\cos\theta}, \tag{4.1}$$

from the most intense (311) XRD peak. β is the full width at half maximum and θ is the Bragg's angle. The D_s values shown in Table 4.1 fluctuate between 8 nm and 16 nm. For the sample $x = 0.3$ the crystallite size is about 9 nm and its XRD spectrum does not show impurity peaks. Crystallite sizes (D_w) can also be estimated from all the major peaks in an XRD spectrum by using the William-Hall (W-H) equation [22]:

$$\beta\cos\theta = \frac{0.91\lambda}{D_w} + 4\varepsilon\sin\theta, \tag{4.2}$$

where β is the full width at half maximum for each XRD peak at Bragg's angle θ, and ε is the lattice strain. Equation (4.2) has the advantage of providing information on internal lattice strain. The values of W-H crystallite size (D_w) obtained from the plots of $\beta\cos\theta$ versus $\varepsilon\sin\theta$ are also shown in Table 4.1 for the $Cu_xMn_{1-x}Fe_2O_4$ ($0 \leq x \leq 0.8$) oxides investigated. The typical $\beta\cos\theta$ versus $\varepsilon\sin\theta$ plots are shown in Figure 4.2 for Cu concentrations x between 0 and 0.4.

Table 4.1: Variation of crystallite size (D), lattice parameter (a), X-ray density (ρ_x) and lattice strain (ε) as a function of Cu content x for $Cu_xMn_{1-x}Fe_2O_4$.

x	D_s(nm)	D_w(nm)	a (Å)	ρ_x(g/cm^3)	ε
	±0.2	±2	±0.001	±0.01	±0.002
0	10.9	13	8.506	4.98	0.001
0.1	15.5	25	8.457	5.08	0.002
0.2	14.4	13	8.425	5.16	0.002
0.3	8.5	8	8.405	5.22	0.005
0.4	14.4	16	8.425	5.20	0.001
0.5	11.5	6	8.412	5.24	0.005
0.6	16.0	15	8.388	5.31	0.001
0.7	8.2	4	8.378	5.35	0.002
0.8	8.3	5	8.343	5.43	0.001

Figure 4.3 shows the D_s and D_w values plotted as a function of Cu content x. The values of crystallite size estimated by equations (4.1) and (4.2) have a similar trend and are not significantly affected by Cu atom concentration. The crystallite size differences observed for samples $x = 0.1$, 0.5, 0.7 and 0.8 shown in Figure 4.3 may be due to the scattered data points on the graphs of $\beta\cos\theta$ versus $\varepsilon\sin\theta$ and anisotropic behaviour.

The values of the lattice strain (ε) deduced from the W-H equation (4.2) are shown in Table 4.1 and they fluctuate between 0.001 and 0.005. Lattice strain is not significantly affected by Cu concentration. The lattice parameters were computed from Miller indices (hkl) and Bragg's angle θ by using the equation [125, 126]:

$$a = \frac{\lambda\sqrt{h^2 + k^2 + l^2}}{2\sin\theta}. \tag{4.3}$$

The lattice constant reduces with increasing Cu concentration according to Vegard's law [120]. This is the law that states that a decreases when a large ion is replaced by a smaller ion in the crystal structure and decreases when a large ion replaces a smaller ion in the crystal structure. The ionic radius of Cu^{2+} is 0.072 nm [121] while the ionic radius of Mn^{2+} (0.083nm) is higher than for Mn^{3+} (0.064 nm) [32]. Hence the reduction of a unit cell with increasing Cu content is attributed to the substitution of larger Mn^{2+} (0.083 nm) ion by smaller Cu^{2+} (0.072 nm) ions.

Both $MnFe_2O_4$ and $CuFe_2O_4$ are inverse spinels where Mn^{2+} and Cu^{2+} ions have a preference for octahedral (B) sites and equal fractions of Fe^{3+} ions are distributed within tetrahedral (A) sites. Doping $MnFe_2O_4$ ferrite with Cu atoms forces Fe^{3+} ions from B- to A-sites [127].

The cation distribution in $Cu_xMn_{1-x}Fe_2O_4$ may be written as [128]:

$$\left[\mathrm{Fe}^{3+}_{1-x}\right]_A \left[\mathrm{Cu}^{2+}_{x}\mathrm{Mn}^{2+}_{1-x}\mathrm{Fe}^{3+}_{1+x}\right]_B O_4. \tag{4.4}$$

This gives A- and B-site radii as [129]:

$$r_A = R_{Fe^{3+}} - xR_{Fe^{3+}} \quad \text{and} \tag{4.5}$$

$$r_B = \frac{1}{2}\left[xR_{Cu^{2+}} + (1-x)R_{Mn^{2+}} + (1+x)R_{Fe^{3+}}\right], \tag{4.6}$$

where $R_{Fe^{3+}}$, $R_{Cu^{2+}}$, and $R_{Mn^{2+}}$, are ionic radii for the respective atoms. The theoretical lattice parameter (a_{th}) can be computed by using the relation [120, 130]:

$$a_{th} = \frac{8}{3\sqrt{3}}\left[(r_A + R_O) + \sqrt{3}(r_B + R_O)\right], \tag{4.7}$$

where r_A and r_B, are A- and B-site radii and R_O (0.132 nm) is the ionic radius of oxygen ion [120]. The theoretical and experimental lattice parameters are depicted in Figure 4.4 as a function of composition. Deviation of experimental values from theoretical ones may be due to deviation of experimental cation distribution in fine particles from inverse spinels in bulk form and the presence of impurity phases [130]. The X-ray density (ρ_x) was calculated from the size of the unit cell (a) by using the equation [120, 129, 131]:

$$\rho_x = \frac{8M}{N_A a^3}, \tag{4.8}$$

where M is a molecular mass, and N_A is Avogadro's constant. The variation of ρ_x as a function of x is shown in Figure 4.5.

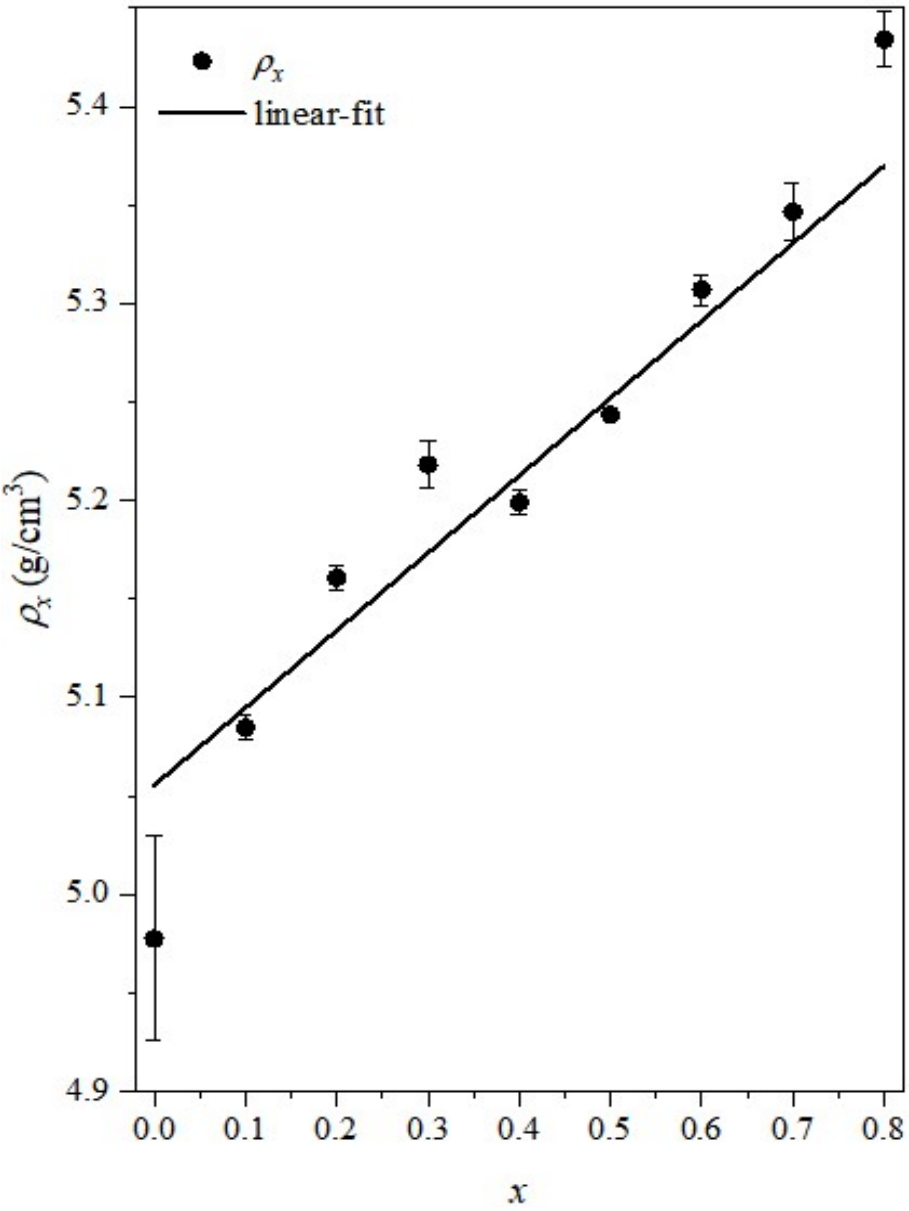

Figure 4.5: Variation of ρ_x as a function of Cu content x for $Cu_xMn_{1-x}Fe_2O_4$ oxides.

The linear increase in ρ_x as a function of composition can be explained by its inverse proportionality to the parameter (a) in equation (4.8). ρ_x reflects on the packing of atoms within the unit cell. Substitution of larger Mn by smaller Cu atoms reduces vacant spaces, hence more close packing of atoms. As shown in Figure 4.1, the sample with composition $Cu_{0.3}Mn_{0.7}Fe_2O_4$ does not show any impurity phases. Hence further magnetization measurements were done for this compound.

4.2.2 Magnetization results

The magnetic properties were investigated using a SQUID magnetometer between 4 K and 400 K. Analysis was done for the sample $x = 0.3$ ($Cu_{0.3}Mn_{0.3}Fe_2O_4$) which did not show impurity phases of α-Fe_2O_3 and Mn_2O_3. The hysteresis loops recorded from 10 K to 400 K in an external magnetic field up to 2 kOe are shown in Figure 4.6. The insert in Figure 4.6 shows the magnified view within a small magnetic field range. Very small coercive fields are indicative of the superparamagnetic nature of the $Cu_{0.3}Mn_{0.7}Fe_2O_4$ fine particles.

The magnetization shows a tendency towards saturation in the magnetic field of 2 kOe. Saturation magnetization (M_s) can be estimated by the equation [13, 132]:

$$M(H) = M_s \left(1 - \frac{a}{H}\right), \tag{4.9}$$

where a/H represents the magnetic hardness term related to structural defects [133]. The values of M_s were obtained from the plots of M versus $1/H$ in the high magnetic field region. A typical plot of M vs $1/H$ is shown in Figure 4.7 for the measurements performed at 10 K. As shown in Figure 4.8, the saturation magnetization reduces with increasing temperature from about 75 emu/g at 10 K to about 50 emu/g at 400 K. This is due to the thermal agitation of the magnetic moments resulting in the random distribution at higher temperatures.

Table 4.2: Variation of saturation magnetization (M_s), remanence magnetization (M_r), coercive field (H_c) and Bohr magneton per unit (n_B) for $Cu_{0.3}Mn_{0.7}Fe_2O_4$ oxides.

T (K)	M_s(emu/g)	M_r(emu/g)	H_c (Oe)	M_r/M_s	n_B
	±0.007	±0.5	±6	±0.007	±0.008
10	74.776	7.2	88	0.151	3.122
50	74.398	3.8	42	0.039	3.107
70	73.628	3.9	45	0.053	3.074
100	72.150	3.7	31	0.051	3.013
150	69.191	0.7	7	0.010	2.889
200	65.907	1.7	17	0.026	2.752
300	55.021	1.0	13	0.018	2.297
400	48.328	0.2×10^{-1}	0.5	4.426×10^{-4}	2.018

The values of saturation magnetization (M_s), remanence magnetization (M_r) and coercive field (H_c) are listed in Table 4.2. According to the Bloch's law, saturation magnetization varies with temperature as [134]:

$$M_s(T) = M_s(0)\left[1 - \left(\frac{T}{T_0}\right)^n\right], \tag{4.10}$$

where $M_s(0)$ is the saturation magnetization at 0 K, T_0 is the temperature in which saturation magnetization is zero, and n is the Bloch's constant. The best fit of the Bloch's law to the experimental data shown by the solid line in Figure 4.8 was obtained with n = 1.4.

Figure 4.9 shows the variation of the coercive field (H_c) as a function of the measuring temperature. The coercive field reduces with the rise in temperature. The higher magnetization and coercive magnetic fields at low temperatures can be explained by the core-shell model as being due to spin freezing [29,135]. In a core-shell nanoparticle, the core spins are in an ordered magnetic phase and the shell spins might be in an enhanced relaxation state (even in a paramagnetic state) because of the broken exchange bonds at the nanoparticle's surface. At low temperatures, shell-spins are frozen into their random states giving small response to the external field. This is

more evident in fine particles. The points are the experimental data, and the solid line is the fitted Kneller's law [134]

$$H_c(T) = H(0)\left[1 - \left(\frac{T}{T_B}\right)^{\beta}\right], \tag{4.11}$$

where $H(0)$ is coercive field at 0 K, T_B is the blocking temperature and β is Kneller's constant [134]. As seen in Figure 4.9, H_c values at 150 K, and 400 K are quite far from the Kneller's fit. The obtained fitting parameters of $T_B = 531 \pm 178$ K and $\beta = 0.4 \pm 0.002$, are a little far from the previously observed values for similar-sized magnetic particles [134]. However, with the included error, β is similar to the normal value reported by the literature (0.5) [134]. The blocking temperature from Kneller's fit disagrees with the one obtained from zero field cooling (120 K). This discrepancy in parameters may be caused by the imperfect fit of experimental data to the proposed law.

The values of the Bohr magneton per unit (n_B) in Table 4.2 were calculated using the relationship [136]:

$$n_B = \frac{M \times M_s}{5585}. \tag{4.12}$$

n_B is proportional to saturation magnetization. Reducing n_B with increasing temperature relates well with saturation magnetization reducing with rising temperature due to increasing thermal energy.

The temperature dependence of spontaneous magnetization is shown in Figure 4.10. Field cooled (FC) and zero field cooled (ZFC) data were recorded from 4 K to 400 K. During the ZFC operation, the sample was cooled in the absence of an external magnetic field from 400 K to 4 K and magnetization data were recorded while warming up the sample in the presence of a 50 Oe external magnetic field. In the FC mode the magnetization was recorded while cooling a sample in the presence of an external magnetic field of 50 Oe. Significant differences are observed between the FC and ZFC curves shown in Figure 4.10.

The ZFC magnetization curve initially increases with increasing temperature and reaches a maximum value at the blocking temperature (T_B) of about 120 K. With further increase in temperature above T_B, the magnetization curve decreases. The "hump" of the ZFC curve is characteristic of the superparamagnetic nature of the sample investigated. The temperature of optimal magnetization (T_B) is related to

the magnetocrystalline anisotropy constant (K) and the volume (V) of the crystalline particles as [137, 138]:

$$T_B = \frac{KV}{25k_B}. \tag{4.13}$$

The initial increase in magnetization with increasing temperature below T_B can be explained by frozen magnetic moments of nanoparticles along the easy axis due to the large anisotropy energy at low temperatures. The nanoparticles gain thermal energy with increasing temperature which opposes the anisotropy energy barrier lead to much easier alignment with the field [137, 139, 140]. The shape of the ZFC curve below T_B reveals the ferrimagnetic behaviour of the sample $Cu_{0.3}Mn_{0.7}Fe_2O_4$ under investigation [138, 139, 141]. Above T_B, the magnetic moments are unblocked because the thermal energy has overcome the anisotropic energy barrier [142, 143]. The decrease in magnetization observed above T_B is attributed to superparamagnetic behaviour of nanoparticles following Curie-Weiss law [144]. The magnetization keeps dropping until the ZFC and FC curves meet at about 257.38 K called the bifurcation temperature. This point of superimposition marks the blocking temperature for the largest superparamagnetic particles [145]. The FC curve appears to be flat (plateau shape) below T_B. This shows spin-glass-like behaviour, indicating strong dipole-dipole interactions among Cu-Mn nanoparticles also observed in other nanoparticles in the literature [139, 141]. Above T_B, magnetization reduces with further increase in temperature due to thermal agitation.

4.3 Conclusion

Nanocrystalline $Cu_xMn_{1-x}Fe_2O_4$ ($0 \leq x \leq 0.8$) have been produced by glycol-thermal reaction and analysed by using XRD and magnetization measurements as a function of temperature under influence of magnetic fields. Small impurity peaks due to α-Fe_2O_3 and α-Mn_2O_3 at $2\theta \approx 52^\circ$ were observed for most samples, except for sample x =0.3 ($Cu_{0.3}Mn_{0.7}Fe_2O_4$). Detailed magnetization analyses were done for this sample with no impurity peaks. The lattice constant reduces with increasing Cu concentration due to smaller Cu- replacing larger Mn atoms. This compares well with the increase in X-ray density observed. Almost zero coercive fields and "S"-shaped magnetization indicate superparamagnetic nanoparticles. This was confirmed by

ZFC magnetization data which also revealed spin-glass behaviour.

Chapter 5

Magnetic properties of (Cd, Zn)$Al_{0.8}Fe_{1.2}O_4$ oxides

5.1 Introduction

$ZnFe_2O_4$ is one of the most studied spinel ferrites due to its exotic electrical and magnetic properties [146]. Enhancement of the magnetic properties of this compound was reported due to the introduction of Al atoms. Zn-Al ferrites showed higher saturation magnetization [147]. $Al_xZnFe_{2-x}O_4$ produced by S. Gul et al. [55] showed superparamagnetic behaviour and a decrease in DC conductivity [55] (essential for low-eddy current losses in transformers) [46]. The magnetic properties of ferrites are influenced by the chemical composition and sample preparation technique. Zn and Cd atoms have similar electron configurations but Cd atoms have a larger size (r_{ionic} = 0.97 Å) than Zn atoms (r_{ionic} = 0.74 Å) [148]. In this project, an attempt was made to compare the magnetic properties of Zn- and Cd- based aluminium ferrites. In this attempt $ZnAl_{0.8}Fe_{1.2}O_4$ and $CdAl_{0.8}Fe_{1.2}O_4$ were synthesized and characterized by using XRD measurements.

5.2 Results and Discussions

5.2.1 X-ray diffraction and TEM results

The XRD patterns for $CdAl_{0.8}Fe_{1.2}O_4$ and $ZnAl_{0.8}Fe_{1.2}O_4$ ferrites are shown in Figure 5.1. The XRD spectrum for the Cd-based sample shows major impurity peaks indicated by an asterisk ($*$) which may be due to α-Fe_2O_3 [120, 149–151]. Only (311), (400), (511) and (440) XRD peaks which are not well crystallized are associated with cubic spinel phase.

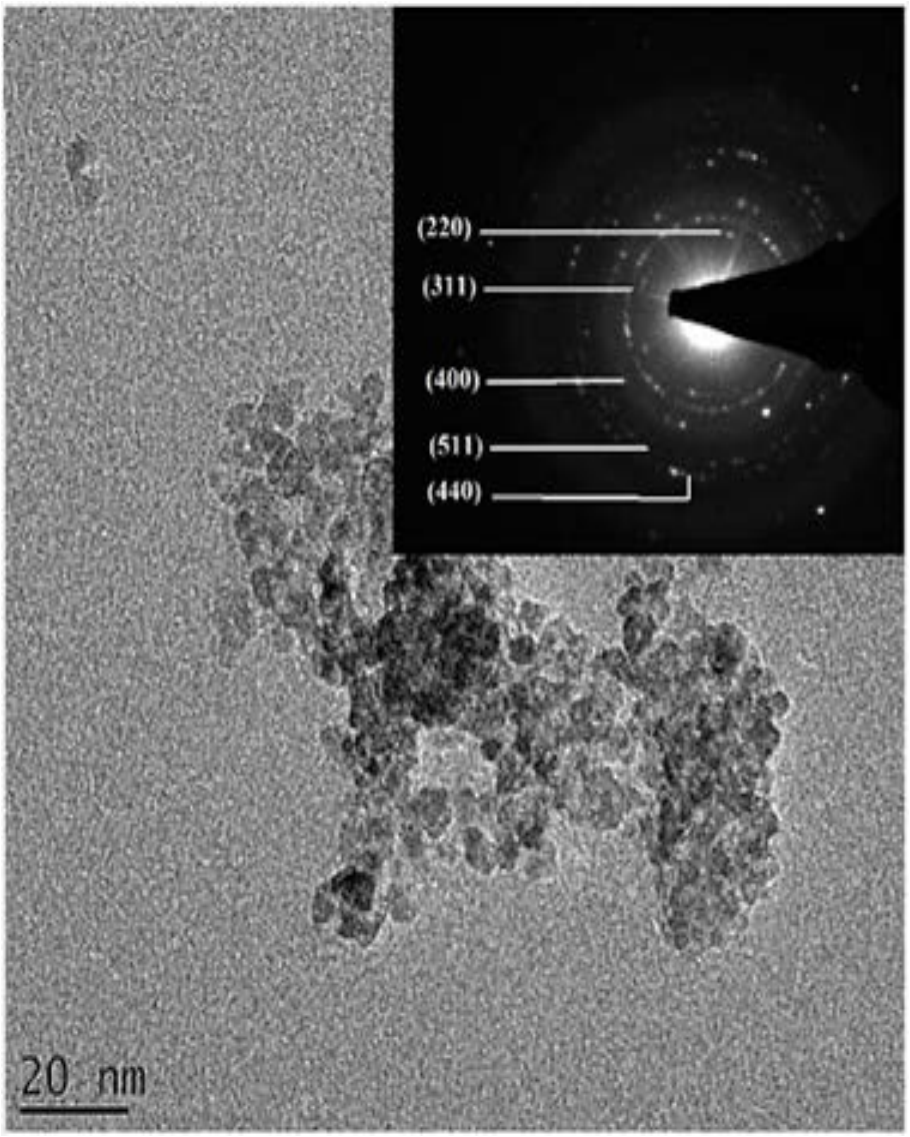

Figure 5.2: TEM micrographs for $ZnAl_{0.8}Fe_{1.2}O_4$ oxide.

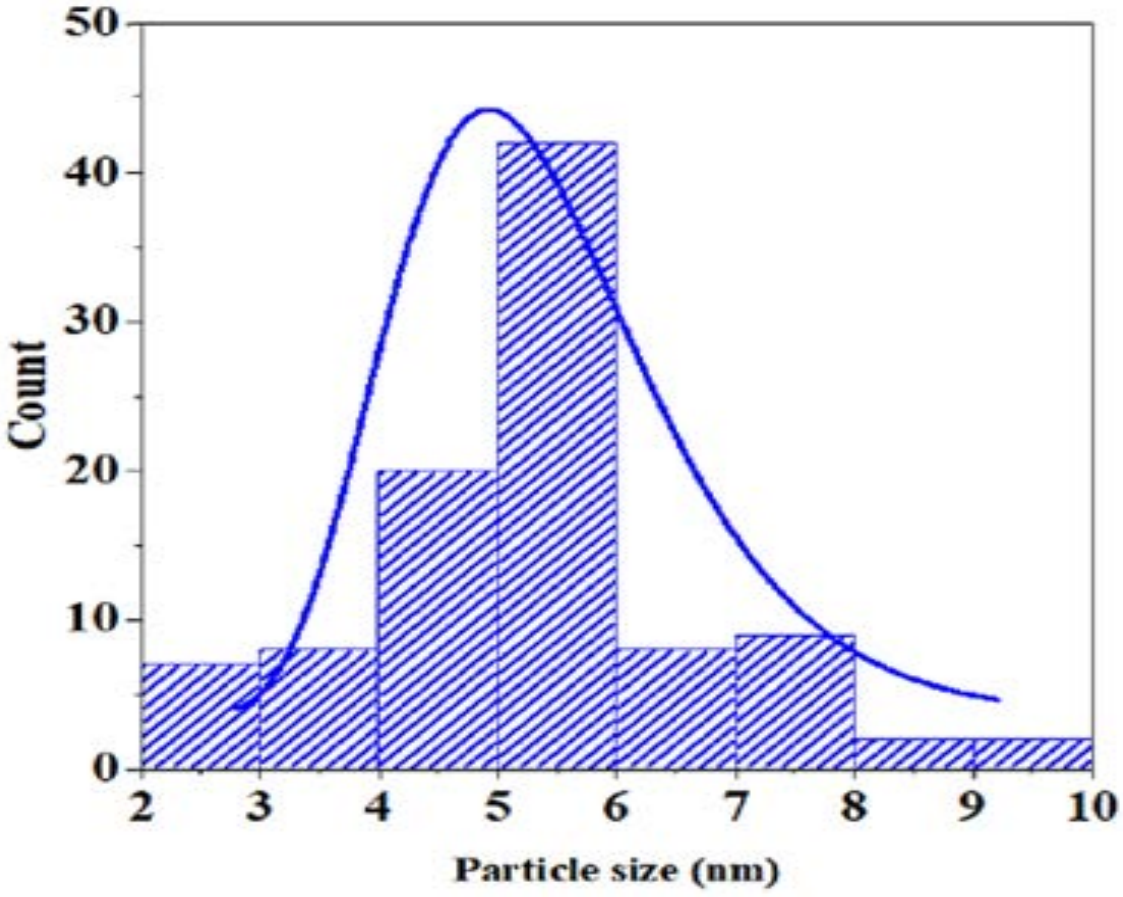

Figure 5.3: Particle size distribution for $ZnAl_{0.8}Fe_{1.2}O_4$ oxide.

A cubic spinel ferrite phase could not be formed for the Cd- based sample. We suspect this to be due to the larger size of Cd atoms. Impurity peaks were observed for Cd- substituted cobalt ferrites [150]. They disappeared after annealing at 700 °C. The spectrum for $ZnAl_{0.8}Fe_{1.2}O_4$ was indexed to the cubic spinel phase with no evidence of impurities. This is confirmed by the (220), (311), (400), (511) and (440) peaks in the XRD spectrum. Results show the ease of sample production with smaller Zn^{2+} than with larger Cd^{2+} ions. Broad XRD peaks for Zn- based compound reveal fine particles.

For the $ZnAl_{0.8}Fe_{1.2}O_4$ oxide, the crystallite size of about 6.6 nm was estimated from the XRD data. Direct measurements of particle size were obtained by using TEM. The TEM image for the Zn-based oxide is shown in Figure 5.2. Almost spherical particles are observed. The particle size distribution shown in Figure 5.3 indicates a narrow particle size distribution with an average particle size of 5±1 nm. This relates well with a value (∼6.6 nm) estimated from XRD data. Further analysis has

been done for the $Zn_{0.8}Fe_{1.2}O_4$ ferrite with no impurity phases.

5.2.2 ESR results

The ESR signal for $ZnAl_{0.8}Fe_{1.2}O_4$ for the as prepared (AP) and annealed samples which did not show any impurity phases is shown in Figure 5.4. The single-line signals for both AP and annealed $ZnAl_{0.8}Fe_{1.2}O_4$ compounds confirm a single phase cubic spinel structure. The narrow signal for the as prepared compound is indicative of dominant superexchange interactions [125]. The Landé g-factor is related to the resonance magnetic field (H_r) as [36]

$$g = \frac{h\nu}{\mu_B H_r}, \tag{5.1}$$

where h is a Plank's constant, ν = microwave frequency and μ_B is the Bohr magneton. It is dependent on molecular motion, paramagnetic properties and symmetry of ions [36]. The g-factor is 2.0023 for a free electron and may be different in a solid environment [45]. For the $ZnAl_{0.8}Fe_{1.2}O_4$ AP oxides, $g = 2.00$ and it increased to about 2.28 after annealing the sample at about 1000 °C. This is associated with the weakening of superexchange interaction and dominance of dipolar interactions [152] in the sample with larger particles.

The full width at half maximum ($\Delta H_{1/2}$) can be computed from the peak-to-peak width (ΔH_{pp}) by using the equation [153]

$$\Delta H_{1/2} = \sqrt{3}\Delta H_{pp}. \tag{5.2}$$

An increase in ΔH_{pp} from 313 G for the AP to about 1855 G for annealed compounds (particle size about 30 nm) associated with the weakening of superexchange interactions and strengthening of dipolar interactions with increase in particle size was observed [32].

The magnetic spin-spin relaxation process is dependent on the magnetic field and the rate at which microwave energy is absorbed or released. Spin-spin relaxation time constant (T) is characteristic of the spin-spin relaxation process. It can be estimated from $\Delta H_{1/2}$ by the expression [131]

$$T_2 = \frac{g\Delta H_{1/2}\mu_B}{\hbar}. \tag{5.3}$$

5.3 Conclusion

An attempt to produce $CdAl_{0.8}Fe_{1.2}O_4$ and $ZnAl_{0.8}Fe_{1.2}O_4$ has been made. The XRD patterns for Cd-based oxide showed impurity phases. $ZnAl_{0.8}Fe_{1.2}O_4$ was successfully produced by glycol-thermal reaction. ESR data confirmed single cubic spinel and dominant superexchange interactions in the AP fine powders. The annealing process has significant effects on electron spin dynamics of $ZnAl_{0.8}Fe_{1.2}O_4$ investigated.

Chapter 6

Magnetic properties of $Ni_xCo_{1-x}Fe_2O_4$ oxides

6.1 Introduction

$CoFe_2O_4$ nanoparticles have exceptional electromagnetic performance, mechanical hardness, chemical stability, high electrical resistivity, high coercive fields and moderate saturation magnetization [2, 125]. Nickel ferrite is a soft magnetic material with applications in technologies like transformer cores, inductors [125], MRI, magnetic fluids, gas sensing, drug delivery etc. [154]. Doping of $CoFe_2O_4$ by Ni favours magnetic transition from ferro- to superparamagnetism [131]. The magnetic properties of Ni-substituted ferrites have been investigated by mössbauer and magnetization measurements [156]. In this chapter, the analysis of $Ni_xCo_{1-x}Fe_2O_4$ with fine particles by ESR spectroscopy is presented.

6.2 Results and Discussions

6.2.1 X-ray diffraction

The XRD patterns for $Ni_xCo_{1-x}Fe_2O_4$ ($0 \leq x \leq 1$) are shown in Figure 6.1. The major peaks were indexed to (220), (311), (400), (422), (511) and (440) confirming a cubic spinel structure [24]. A small impurity peak at about $2\theta = 52^\circ$ which becomes significant for compositions with $0.7 \leq x \leq 0.9$ has been observed. This peak may be due to iron or nickel oxide impurity phases [157]. The broad peaks for these patterns are evidence of fine particles. Table 6.1 shows the values of crystallite sizes (D_s and D_w) calculated from the XRD data as discussed in Chapter 4, section 4.1. During sample preparation, the reaction temperature was kept constant in a pressure reactor for five hours. The pressure was allowed to increase to a maximum which varied for different reactions. This parameter which is one of the reaction conditions might have contributed to the variation of particle size.

Table 6.1: D_s, D_w, a, ρ_x and ε as a function of Ni content x.

x	D_s(nm)	D_w(nm)	a (Å)	ρ_x(g/cm^3)	ε
	±0.1	±1	±0.004	±0.01	±0.002
0	9.5	11	8.322	5.39	0.002
0.1	11.0	11	8.378	5.31	0.0001
0.2	6.9	11	8.382	5.31	0.002
0.3	10.2	10.1	8.380	5.29	0.0002
0.4	7.9	7.0	8.369	5.22	0.001
0.5	12.7	11.3	8.375	5.33	0.0003
0.6	7.6	6	8.375	5.31	0.002
0.7	8.2	6	8.376	5.34	0.006
0.8	6.9	8	8.366	5.33	0.001
0.9	6.9	5	8.357	5.35	0.0004
1	10.5	9	8.355	5.34	0.0004

Figure 6.2 shows the variation of the lattice parameter as a function of nickel concentration. The experimental values of the size of a unit cell (lattice constants) are not significantly affected by Ni ion concentration x. This may be due to the similar size of Ni ($r_{ionic} = 0.72$Å) and Co ($r_{ionic} = 0.76$Å) [158] ionic radii. The distribution of metal cations for $Ni_xCo_{1-x}Fe_2O_4$ may be written as $[Ni_xFe]_A[Co_{1-x}Fe]_BO_4$ [129].

This gives sites radii [129]:

$$r_A = R_{Fe^{3+}} + xR_{Ni^{2+}} \quad \text{and} \tag{6.1}$$

$$r_B = \frac{1}{2}\left[(1-x)R_{Co^{2+}} + R_{Fe^{3+}}\right], \tag{6.2}$$

where R is the ionic radius of an atom. Hence the theoretical lattice parameters were calculated from r_A and r_B using equation (4.7) in Chapter 4. As shown in Figure 6.2, a reduction in theoretical lattice parameters as a function of Ni content occurs. This may be explained by the assumption that all Co atoms are on B- sites and Ni atoms on A-sites which is not true. Both Ni^{2+} and Co^{2+} ions are known to have a preference for B-sites [159].

6.2.2 Electron spin resonance measurements

The ESR analyses of $Ni_xCo_{1-x}Fe_2O_4$ nanoferrites were carried out at room temperature ($\sim$ 300 K). The variation of ESR spectra as a function of magnetic field for different compositions is shown in Figure 6.3. The ESR signals are initially broad and become narrow as Ni concentrations x is increased. Resonance peaks occurs at fields between 2 kG and 8 kG for lower Ni concentrations x. These peaks shift to lower magnetic fields as Ni concentration increases. Additional resonance signals are observed at low magnetic fields for samples $0.1 \leq x \leq 0.8$. The ESR signals at very low magnetic fields close to 0 kG may be attributed to LFMA [82]. This is a recent phenomenon that is not yet fully understood in magnetic materials [79].

Resonant magnetic field (H_r) and peak-to-peak (ΔH_{pp}) values are listed in Table 6.2. These give information on the magnetic dipolar interaction, superexchange interactions and spin-spin relaxation behaviour of the magnetic nanoparticles [153]. The reduced values of linewidth as a function of Ni concentration were caused by strengthening of superexchange interactions and weakening of dipolar interactions [37, 45]. Values of Landé g-factor also shown in Table 6.2 were deduced from measured H_r values as discussed in section 5.2.2.

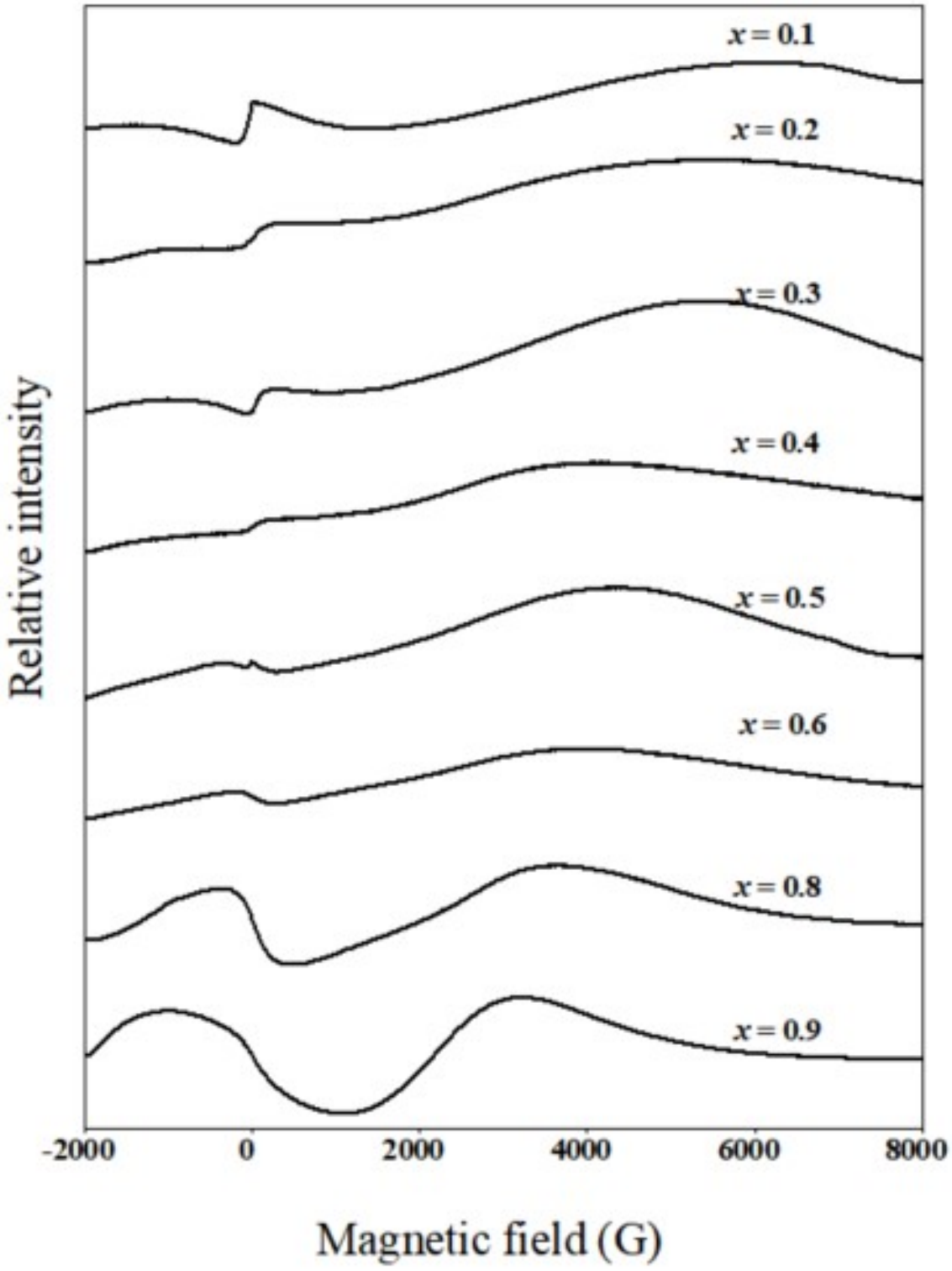

Figure 6.3: ESR spectra for $Ni_xCo_{1-x}Fe_2O_4$ ferrites as a function of magnetic field for different compositions.

The g-factors are dependent on a solid environment and are affected by magnetic dipole and superexchange interactions between magnetic spins through intervening oxygen ions. The calculated values range between 1.9 and 3.6. The minimum value of g indicates the value of x at which the superexchange interaction is the strongest [153]. The spin-spin relaxation time reduces from 0.706 femtoseconds (fs) for sample $x = 0.1$ to 0.104 fs for sample $x = 0.9$ with the highest concentration of Ni^{2+}. Nickel content appears to favour atoms' spin-spin relaxation.

Table 6.2: The ESR parameters of $Ni_xCo_{1-x}Fe_2O_4$ oxides.

x	H_r(G)	ΔH_{pp}(G)	g	$T_2 \times 10^{-15}$(s)
	± 15	± 5	± 0.00001	± 0.001
0.1	3391	4700	1.97805	0.706
0.2	2598	4647	2.58177	0.547
0.3	2863	4485	2.34250	0.625
0.4	1889	3695	3.55170	0.500
0.5	2102	3973	3.19067	0.518
0.6	1948	3692	3.44382	0.516
0.8	2284	3012	2.93617	0.742
0.9	2261	2123	2.96650	0.104

6.3 Conclusion

Glycol-thermally prepared oxides of composition $Ni_xCo_{1-x}Fe_2O_4$ ($0.1 \leq x \leq 1$) were studied using ESR measurements. The XRD results revealed the successful formation of the spinel phase with major peaks corresponding to cubic spinel. Nanosized particles of crystallite sizes between about 6 and 13 nm were formed. The strengthening of superexchange interaction through the introduction of nickel in $Ni_xCo_{1-x}Fe_2O_4$ was observed from ESR analyses.

Chapter 7

Magnetic properties of $Cu_{0.5}Ni_{0.5}Fe_2O_4$ nanoferrites

7.1 Introduction

$CuFe_2O_4$ is a fascinating material due to its amazing intrinsic magnetic and semiconducting properties [160]. These include high coercivity, large magnetocrystalline anisotropy, moderate saturation magnetization and large room temperature magnetostrictive coefficient [119]. Nickel doping has softening properties that lead to modifications of electrical and magnetic properties of ferrites. A combination of Ni and Cu ions in a spinel structure can give improved electrical and magnetic properties. Annealing temperature also plays an important role in altering the physical properties of ferrites. In this chapter, the effect of particle size on the magnetic properties of a compound with composition $Cu_{0.5}Ni_{0.5}Fe_2O_4$ has been investigated. The effect of annealing temperature on structural properties of these materials have been studied through XRD. A more detailed information on the effect of annealing temperature to the structural properties of these ferrites have been provided. The dependence of magnetic properties on annealing temperature studied using ESR measurements are presented in this chapter.

7.2 Results and Discussions

7.2.1 X-ray diffraction

Figure 7.1 shows the XRD patterns for $Cu_{0.5}Ni_{0.5}Fe_2O_4$ compounds for the as-prepared (AP) and samples annealed from 500 °C to 1100 °C. The major diffraction peaks confirm cubic spinel [129, 131, 132]. The broad diffraction peaks are attributed to fine particles [131, 161]. The narrowing of peak width and an increase in intensity with an increasing annealing temperature indicate increasing particle size [131, 134, 162].

Table 7.1 shows D_s, D_w, a, ρ_x and ε as a function of annealing temperature. The values of D_s calculated from the standard Debye-Scherrer equation range from about 12 nm to 34 nm after annealing at 1100 °C. The increase in crystallite sizes with annealing temperature indicates grain growth caused by annealing processes [134,162].

Table 7.1: Ds,D_w, a, ρ_x and ε for $Cu_{0.5}Ni_{0.5}Fe_2O_4$ oxides

T (°C)	D_s(nm)	D_w(nm)	a (Å)	ρ_x(g/cm^3)	ε
	±0.4	±1	±0.001	±0.004	±0.001
AP	11.7	9	8.308	5.519	0.002
500	12.8	11	8.331	5.474	0.0002
700	11.8	12	8.334	5.469	0.0001
800	12.8	13	8.323	5.499	0.001
900	45.6	34	8.391	5.490	0.001
1000	32.3	26	8.391	5.358	0.0007
1100	33.7	31	8.360	5.418	0.0004

Figure 7.2 (a) and (b) show TEM micrographs for $Cu_{0.5}Ni_{0.5}Fe_2O_4$ ferrites annealed at 800 and 900 °C respectively. The particles are almost spherical in shape. The selected area electron diffraction (SAED) patterns are shown on the inserts of each TEM micrograph. The sharp dotted SAED patterns indicate the polycrystalline nature of particles with indices of a spinel structure [125, 136, 145, 159]. The average grain-sizes (D_{TEM}) of about 18 nm for the samples annealed at 800 and 900 °C were obtained. Figure 7.3 shows the particle size distributions for samples annealed at (a) $T = 800$ °C and (b) $T = 900$ °C.

A general reduction in ε with increasing annealing temperature is reflected in Table 7.1. This relates well with increasing particle sizes which can be associated with more vacant spaces and hence smaller strain in the crystal lattice [163]. As shown in Table 7.1, the ρ_x values relate well with the ε. For the as-prepared compound $\rho_x = 5.519$ g/cm^3 and $\varepsilon = 0.002$ while for the sample annealed at 1100 °, $\rho_x = 5.418$ g/cm^3 and a lower value of strain 0.0004 is observed. Lower values of strain compare

7.2.2 Electron spin resonance measurements

The typical room temperature ($\sim$ 300 K) electron spin resonance spectra for the AP samples and samples annealed at 800 °C and 900 °C are shown in Figure 7.4. Changes in particle size have significant effects on the ESR signal. The AP sample produced under a low reaction temperature of 200 °C with particle size of about 12 nm has a lower intensity than the $Cu_{0.5}Ni_{0.5}Fe_2O_4$ compounds annealed at 800 °C and 900 °C.

The compound annealed at 900 °C which has larger crystallite sizes of about 45 nm has a maximum intensity. This could be due to maximum magnetization for this sample [36] due to ferromagnetic gains. Crystallite size also influences the positions of the ESR signals. The compound with larger particle sizes has a lower resonance magnetic field of about 2.032 kG as compared to about 2.445 kG for the AP sample as seen in Figure 7.4. This behaviour of magnetization can be explained in terms of the core-shell spin model [164]. The smaller-sized magnetic nanoparticles have a core-shell spin structure in which randomly oriented surface spins are more dominant than the ferrimagnetically ordered core spins. The randomly oriented surface spins result in reduction of the net magnetic moment of each grain, hence decreased net magnetization of the sample. As the grain sizes increase, there are more ferrimagnetically ordered spins in the core of the core-shell structure, resulting to enhanced magnetization for larger particle sizes [165].

Table 7.2 shows ESR parameters obtained from ESR spectra for $Cu_{0.5}Ni_{0.5}Fe_2O_4$. The peak-to-peak linewidth and Landé-g factor are dependent on the superexchange interaction between magnetic cations via a non-magnetic oxygen anion and dipole-dipole interactions [161]. The dominance of dipole-dipole interaction causes enhancement of the Landé-g factor and peak to peak line width whereas the strengthening of superexchange interaction leads to a decrease in these parameters [37,131]. The large values of Landé-g factor ($\sim$3) for both annealed and as-prepared samples indicate very weak superexchange interactions for these nanoferrites.

The relaxation time gives information about the absorption and dissipation of electromagnetic radiation energy [36]. It is inversely proportional to specific loss power (SLP) in magnetic hyperthermia.

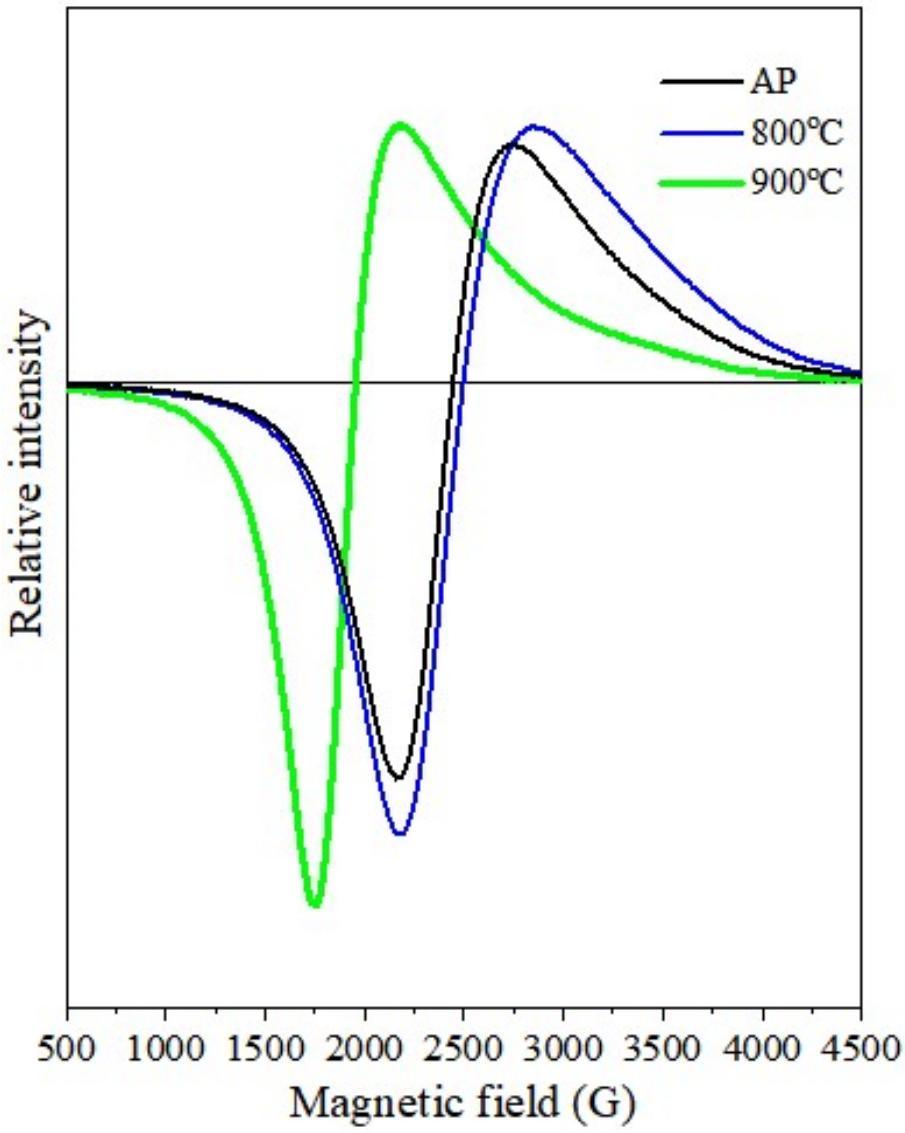

Figure 7.4: ESR Spectra for the AP $Cu_{0.5}Ni_{0.5}Fe_2O_4$ (black) and samples annealed at 800 °C (blue) and 900 ° C (green).

The relaxation time for the nanoparticles in these ferrites was found to be about 4×10^{-11} s as seen in Table 7.2. J. Massoudi et al. [164] have reported a relaxation time in the range of $\sim$ (3-6)$\times10^{-11}$ s for Zn-Al substituted nickel ferrite nanoparticles at various annealing temperatures, making them good candidates for hyperthermia treatment.

Table 7.2: The ESR parameters of $Cu_{0.5}Ni_{0.5}Fe_2O_4$ oxides

T (°C)	H_r(G)	H_{PP}(G)	g	$T_2 \times 10^{-11}$(s)
	$\pm$53	$\pm$2	$\pm$0.07	
200	2445	594	2.74	4.02689
800	2499	697	2.68	3.50758
900	2032	510	3.30	3.89842

7.3 Conclusion

Particle size appear to have significant effects on the ESR signal for the $Cu_{0.5}Ni_{0.5}Fe_2O_4$ samples investigated. An increase in the signal intensity with annealing temperature associated with enhanced magnetization has been observed. A lower resonant magnetic field occurs for samples with larger particles.

Chapter 8

Conclusions and future studies

Nanostructured ferrites with chemical compositions $Cu_xMn_{1-x}Fe_2O_4$, $ZnFe_{1.2}Al_{0.8}O_4$, $Ni_xCo_{1-x}Fe_2O_4$ and $Cu_{0.5}Ni_{0.5}Fe_2O_4$ have been successfully prepared by glycol-thermal reaction. This was confirmed by X-ray diffraction data which showed the major peaks which could be indexed to a single-phase cubic spinel structure. Unlike the $ZnFe_{1.2}Al_{0.8}O_4$ sample, the $CdFe_{1.2}Al_{0.8}O_4$ could not be produced. The XRD spectrum of the Cd-based composition had many impurity phases. This has been attributed to the larger size of Cd atoms. The results show easier formation with smaller Zn atoms.

The compounds have been characterized by XRD, TEM and the magnetic properties have been studied magnetization and ESR measurements. $Cu_xMn_{1-x}Fe_2O_4$ fine particles (particle size between 5nm and 25 nm) were produced. XRD spectra showed small impurity peaks attributed to α-Fe_2O_3 and α-Mn_2O_3 at $2\theta \approx 52^\circ$ for samples $x = 0.1, 0.2, 0.4, 0.5$ and 0.7. The major peaks were indexed to a single-phase cubic spinel structure. Reducing lattice parameters as a function of increasing Cu concentration could be explained by smaller Cu replacing larger Mn ions. Magnetisation measurements were performed for sample $x = 0.3$ ($Cu_{0.3}Mn_{0.7}Fe_2O_4$) which did not have any impurities. Very low coercive fields and a hump in zero field magnetization data revealed the superparamagnetic nature of the $Cu_xMn_{1-x}Fe_2O_4$ investigated.

An attempt to produce (Cd, Zn)$Al_{0.8}Fe_{1.2}O_4$ was made. The Zn-based compounds ($ZnAl_{0.8}Fe_{1.2}O_4$) crystallized with single phase cubic spinel structure while the Cd-based sample did not form. TEM images revealed nearly spherical particles for the Zn-based compound which were characterized by ESR measurements. An additional small resonance signal was observed for the Zn-based compound annealed at 1000 °C. This may be due to the LFMA phenomenon which is not yet fully understood in magnetic materials. This requires further studies as a function of low temperature measurements. ESR studies were also carried out for $Ni_xCo_{1-x}Fe_2O_4$ in search of low field microwave phenomenon. Small resonance signals between -500 G and +500 G were also observed.

Nanosized $Cu_{0.5}Ni_{0.5}Fe_2O_4$ ferrite with a particle size of about 12 nm was produced. This compound was subjected to the annealing processes from 500 °C to 1100 ° in order to investigate the effect of particle size on the magnetic properties. An increase in particle size from about 12 nm to 34 nm occurred after annealing at 1100 °C. Particle size has significant effects on magnetic properties. An increase in signal intensity associated with the enhancement of magnetization was observed.

Future studies

The single phased cubic spinel could not be formed for the Cd- based compounds. Similar results have been observed previously. It will be important to investigate this further using other techniques such as high energy ball milling. ESR studies were performed at room temperature in this study. Low temperature measurements need to be carried out in ferrite materials to confirm the novel low field microwave absorption phenomenon that was observed in some of the materials presented in this dissertation. Further ESR measurements can be performed at lower temperatures to study LFMA phenomenon. It will also be critical to carry out a systematic study of the evolution of the electron spin dynamics as a function of particle size.

Bibliography

[1] G. Aravind, M. Raghasudha and D. Ravinder. *J. Magn. Magn. Mater.*, 378:278, 2015.

[2] V. Kumar H. Kaur, A. Singh and D. S. Ahlawat. *J. Magn. Magn. Mater.*, 474:505, 2019.

[3] L. E. De Leon-Prado, D. A. Cortes-Hernández, J. C. Escobedo-Bocardo, J. Sanchez, P. Y. Reyes-Rdz, R. A. Jasso-Teran and G. F. Hurtado-Lopez. *J. Magn. Magn. Mater*, 427:230, 2017.

[4] R. A. Jasso-Teran, D. A. Cortes-Hernandez, H. J. Sanchez-Fuentes, P. Y. Reyes-Rodriguez, L. Elena de Leon-Prado, J. C. Escobedo-Bocardo and J. M. Almanza-Robles. *J. Magn. Magn. Mater*, 247:241, 2017.

[5] J. Z. Msomi, W. B. Dlamini, T. Moyo and P. Ezekiel. *J. Magn. Magn. Mater.*, 373:68, 2015.

[6] R. Sharma, P. Thakur, P. Sharma and V Sharma. *J. Alloy. Compd.*, 704:7, 2017.

[7] T. R. Tatarchuk, N. D. Paliychuk, M. Bououdina, B. Al-Najar, M. Pacia, W. Macyk and A. Shyichuk. *J. Magn. Magn. Mater.*, 731:1256, 2018.

[8] S. Noor, M. A. Hakim, S. S. Sikder, S. M. Hoque, M. K. Hanium and P. Nordblad. *J. Phys. Chem. Solids*, 73:227, 2012.

[9] M. K. Bharti, S. Gupta, S. Chalia, P. Thakur, I. Garg and A. Thakur. *J. Supercond. Nov. Magn.*, 33:3651, 2020.

[10] T. M. Hamad, S. Kuhn, A. A. Amsha, N. K. Hejazy and R.Hampelmann. *J. Supercond. Nov. Magn.*, 33:3065, 2020.

[11] Y. Ying, L. Wang, W. Li, L. Qiao, J. Zheng, Y. Yu, W. Cai, L. Jiang, S. Che, L. Zhang and L. Ling. *J. Supercond. Nov. Magn.*, 31:3553, 2018.

[12] R. C. Kambale, P. A. Shaikh, S. S. Kamble and Y. D. Kolekar. *J. Alloy. Compd.*, 498:599, 2009.

[13] S. U. Rather and O. M. Lemine. *J. Alloy. Compd.*, 812:12058, 2020.

[14] M. H. Yousefi S. Manouchehri, S. T. M. Benehi. *J. Supercond. Nov. Magn.*, 29:2179, 2016.

[15] S. F. Mansour N. S. Al-Bassami and M. A. Abdo. *J. Supercond. Nov. Magn.*, 33:3077, 2020.

[16] J. P. Rourke M. T. Weller P. W. Atkins, T. L. Overton and F. A. Armstrong. *Shriver & Atkins´ Inorganic chemistry*, pages 82–83. Oxford University Press, 5 edition, 2010.

[17] C. E. Housecroft and A. G. Sharpe. *Inorganic Chemistry*, pages 398–399. Pearson Education Limited, 4 edition, 2012.

[18] E. Swatisang, S. Phokha, S. Hunpratub, B. Usher, A. Bootchanont, S. Maensiri and P. Chindaprasirt. *J. Alloy. Compd.*, 664:792, 2016.

[19] M. A. Almessiere, Y. Slimani, S. Guner, M. Nowaz, A. Baykal, F. Aldakheel, A. Sadaqat and I. Ercan. *J. Mol. Struct.*, 1195:269, 2019.

[20] Y. Zou, H. Wang, R. Yang, X. Lai, J. Wan, G. Lin and D. Liu . *Sens. Actuators, B*, 73:227, 2019.

[21] C. E. Housecroft and A. G. Sharpe. *Inorganic Chemistry*, page 1045. Pearson Education limited, 4 edition, 2012.

[22] J. N. P. K. Chintala, S. Bharadwaj, M. C. Varma and G. S. V. R. K. Choudary). *J. Phys. Chem. Solids*, 160:110298, 2022.

[23] Y. Zheng, G. Hussain, S. Li, S. Batool and X. Wang. *Nanomaterials*, 12:2839, 2022.

[24] S. Rather, H. S. Bamufleh and H. Alhumade. *Ceram. Int.*, 47:17361, 2021.

[25] J. Yao, X. Li, Y. Li and S. Le. *Integr. Ferroelectr.*, 145:17, 2013.

[26] Keyvan Malaie and Mohammad Reza Ganjali. *Journal of Energy Storage*, 33:102097, 2021.

[27] D. S. Nikam, S. V. Jadhav, V. M. Khot, R. A. Bohara, C. K. Hong, S. S. Mali and S. H. Pawar. *RSC Adv.*, 5:2338, 2015.

[28] H. S. Tamayo, K. E. García and C. A. Barrero. *J. Magn. Magn. Mater.*, 471:242, 2019.

[29] H. M. I. Abdallah, T. Moyo, J. Z. Msomi. *J. Supercond. Nov. Magn.*, 25:2625, 2011.

[30] M. A. Njoroge, N. M. Kirimi and K. P Kuria. *Critical Reviews in Solid State and Materials Sciences*, 0:1, 2021.

[31] C. Sun Q. Ni C. Wang Z. Sun, Y. Zao and H.Jin. *Chem Eng. J.*, 431:133448, 2022.

[32] M. Deepty, C. Srinivas, K. V. Babu, E. R. Kumar, S. S. Meena, C. L. Prajapat, N. K. Mohan and D. L. Santry. *J. Magn. Magn. Mater.*, 466:60, 2018.

[33] X. Li, Y. Sun, Y. Zong, Y. Wei, X. Liu, X. Li, Y. Peng and X. Zheng. *J. Alloy. Compd.*, 841:155710, 2020.

[34] I. Sharifi and H. Shokrollahi. *J. Magn. Magn. Mater.*, 324:2397, 2012.

[35] M. Amiri, M. Salavati-Niasari and A. Akburi. *Adv. Colloid Interface Sci.*, 265:29, 2019.

[36] J. Z. Msomi, T. Moyo, S. Mahule and V. V. Srinivasu. *J. Supercond. Nov. Magn.*, 32:1817, 2019.

[37] K. Pubby, K. V. Babu and S. B. Narang. *Mater. Sci. Eng., B*, 255:114513, 2020.

[38] M. B. Shelar and S. M. Patange. *Mater. Today:. Proc.*, 59:1196, 2022.

[39] M. Atif, M. W. Asghar, M. Nadeem, W. Khalid, Z. Ali and S. Badshah. *J. Phys. Chem. Solids*, 123:36, 2018.

[40] R. Sai, S. D. Kulkarni, S. S. M. Bhat, N. G. Sundaram, N. Bhat and S. A. Shivashankar. *RSC Adv.*, 5:10267, 2015.

[41] P. Atkins, T. Overton, J. Rourke, M. Weller, F. Armstrong, and M. Hagerman. *Shriver & Atkins´ Inorganic Chemistry*, page 503. Oxford University Press, 5 edition, 2010.

[42] R. Ahmad, I. H. Gul, M. Zarrar, H. Anwar, M. B. Niazi and A. Khan. *J. Magn. Magn. Mater.*, 405:28, 2016.

[43] V. J. Angadi, L. Choudhury, K. Sadhana, H. Liu, R. Sandhya, S. Matteppanavar, B. Rudraswamy,V. Pattar, and R. V. Anavekar and K. Praveena. *J. Magn. Magn. Mater.*, 424:1, 2017.

[44] S. T. Assar and H. F. Abosheiasha. *J. Magn. Magn. Mater.*, 374:264, 2015.

[45] K. K. Bamzai, G. Kour, B. Kaur, M. Arora and R. P. Pant. *J. Magn. Magn. Mater.*, 345:255, 2013.

[46] T. K. Bromho, K. Ibrahim, H. Kabir, M. M. Rahman, K. Hasan, T. Ferdous, H. Taha, M. Altarawneh and Z. Jhiang. *Mater. Res. Bull.*, 97:444, 2018.

[47] M. Buchner, K. Höfler, B. Henne, V. Ney and A. Ney. *J. Appl. Phys.*, 124:161101, 2018.

[48] C. B. K. Naidu, S. Prathab and W. Madhuri. *J. Supercond. Nov. Magn.*, 33:417, 2020.

[49] J. Chand, G. Kumar, S. K. Sharma, M. Knobel and M. Singh. *J. Alloy. Compd.*, 509:9638, 2011.

[50] K. C. B. Naidu and W. Madhuri. *Mater. Chem. Phys.*, 181:432, 2016.

[51] T. Dippong, O. Cadar, E. A. Levei and I. G. Deac. *J. Magn. Magn. Mater.*, 498:16618, 2020.

[52] W. B. Dlamini, J. Z.Msomi and T. Moyo. *J. Magn. Magn. Mater.*, 373:78, 2015.

[53] R. Ghasemi, J. Echeverria, J. I. P. Landazabal and J. J. B. Lopez. *J. Magn. Magn. Mater.*, 499:166201, 2020.

[54] M. P. Ghosh and S. Mukherje. *J. Magn. Magn. Mater.*, 499:166185, 2020.

[55] S. Gul, M. A. Yousuf, A. Anwar, M. F. Warsi, P. O. Agboola, I. Shakir and M. Shahid. *Ceram. Int.*, 46:14195, 2020.

[56] M. A. Hakim, S. K. Nath, S. S. Sikder and K. H. Maria. *J. Phys. Chem. Solids*, 74:1316, 2013.

[57] J. H. Hankiewicz, J. A. Stoll, J. Stroud, J. Davison, K. L. Livesey, K. Tvrdy, A. Roshko,S. E. Russek, K. Stupic, P. Bilski, R. E. Camley and Z. J. Celiski. *J. Magn. Magn. Mater.*, 469:550, 2019.

[58] V. G. Harris and V. Šepelák. *J. Magn. Magn. Mater.*, 465:603, 2018.

[59] A. Hassan, M. A. Khan, M. Shadid, M. Asghar, I. Shakir, S. Naseem, S. Riaz and M. F. Warsi. *J. Magn. Magn. Mater.*, 393:56, 2015.

[60] J. Chand, S. Verma and M. Singh. *J. Alloy. Compd.*, 552:264, 2013.

[61] A. K. Nandanwar, D. L. Chaodhary, S. N. Kamde, D. S. Choudhary and K. G. Rewatkar. *Mater. Today: Proceedings*, 29:951, 2020.

[62] S. Zare, A. A. Ati, S. D. Dabagh, R. M. Rosnan and Z. Othaman. *J. Mol. Struct.*, 1089:25, 2015.

[63] H. M. Zaki, S. H. AL-Heniti and M. M. Aljwiher. *Physica B*, 597:412382, 2020.

[64] A. Singh, S. Pathak, P. Kumar, P. Sharma, A. Rathi, G. A. Basheed, K. K. Maurya and R. P. Pant. *J. Alloy. Compd.*, 493:65737, 2020.

[65] M. W. Mukhtar, M. Irfan, I. Ahmad, I. Ali, M. N. Akhtar, M. A. Khan, G. Abbas, M. U. Rana, A. Ali and M. Ahmad. *J. Magn. Magn. Mater.*, 381:173, 2015.

[66] O. Kaman, J. Kulickova, V. Herynek, J. Koktan, M. Marysko, T. Dedourkova, K. Knizek and Z. Jirak. *J. Magn. Magn. Mater.*, 427:251, 2017.

[67] Y. Gao, Y. Zhao, Q. Jiao and H. Li. *J. Magn. Magn. Mater.*, 341:93, 2013.

[68] A. Voigt P. Pulišova, J. Kovác and P. Raschman. *J. Magn. Magn. Mater.*, 341:93, 2013.

[69] A. Chaudhuri F. Nayeem, A. Parveez and R. R. S. A. Khader. *Mater. Today: Proceedings*, 4:12138, 2017.

[70] E. Petrova, D. Kotsikau, V. Pankov and A. Fahmi. *J. Magn. Magn. Mater.*, 473:85, 2019.

[71] R. Rai, K. Verma, S. Sharma, S. S. Nair, M. A. Valente, A. L. Kholkin and N. A. Sobolev. *J. Alloy. Compd.*, 509:7585, 2011.

[72] M. Naseri. *J. Magn. Magn. Mater.*, 392:107, 2015.

[73] U. B. Sontu, V. Yalasani and V. R. R. Musungu. *J. Magn. Magn. Mater.*, 374:376, 2015.

[74] A. K. Sijo, V. K. Jha, L. S. Kaykan and D. P. Dutta. *J. Magn. Magn. Mater.*, 497:166047, 2020.

[75] J. Ren, Z. Zhang, X. Ma, Y. Zhong, J. Zhang, Z. Ren and Y. Liu. *J. Magn. Magn. Mater.*, 495:165832, 2020.

[76] A. M. Wahba and M. B. Mohamed. *J. Magn. Magn. Mater.*, 378:246, 2015.

[77] A. A. El-Fadl, A. M. Hassan, M. H. Mahmoud, T. Tatarchuk, I. P. Yeremiy, A. M. Gismelssed and M. A. Ahmed. *J. Magn. Magn. Mater.*, 471:192, 2019.

[78] N. Rezaei, M. H. Ehsani, M. Aghazadeh and I. Karimzadeh. *J. Supercond. Nov. Magn.*, 31:2139, 2018.

[79] T. S. Mahule, V. V. Srinivasu and J. Das. *Solid State Commun.*, 243:60, 2016.

[80] B. Sibanda, T. S. Mahule , D. Delmonte, A. Sala, E. Gilioli, V. V. Srinivasu. *Mater. Res. Express*, 8:066101, 2021.

[81] R. Valenzuela, S. Ammar, S. Nowak and G. Vazquez. *J. Supercond. Nov. Magn.*, 25:2389, 2012.

[82] R. B. Onyancha, J. Shimoyama, J. Das, H. Ogino, H. Ogino, U. O. Aigbe and V. V. Srinivasu. *Solid State Commun.*, 307:113800, 2020.

[83] R. A. Serway and J. W. Jewett Jr. *Physics for Scientists and Engineers with Modern Physics*, pages 786–789. Brooks/Cole Cengage Learning, 10 edition, 2014.

[84] J. M. D. Coey. *Magnetism and Magnetic Materials*, pages 63–67. Cambrige University Press, 1st edition, 2009.

[85] R. Eisberg and R. Resnick. *Quantum Physics of Atoms, Molecules, Solids, Nuclei and Particles*, pages 267–274. John Wiley & Sons,inc, 2 edition, 1985.

[86] W. D. Jr. Callister and D. D. Rethwisch. *Materials Science and Engineering*, pages 803–815. John & Sons, Inc., 9 edition, 2014.

[87] D. Jiles. *Introduction to Magnetism and Magnetic Materials*, pages 221–244. CRC Press, Tailor & Francis group, 3 edition, 1991.

[88] B. D. Cullity and C. D. Graham. *Introduction to Magnetic Materials*, pages 89–162. John Willey & Sons, inc., 2 edition, 2009.

[89] D. Jiles. *Introduction to magnetism and Magnetic Materials*, pages 81–82. Chapman and Hall, 1 edition, 1991.

[90] C. E. Housecroft and A. G. Sharpe. *Inorganic chemistry*, pages 705–707. Pearson Education limited, 4 edition, 2012.

[91] P. W. Atkins, T. L. Overton, J. P. Rourke, M. T. Weller and F. A. Armstrong. *Shriver & Atkins´ Inorganic chemistry*, pages 502–505. Oxford University Press, 4 edition, 2010.

[92] R. Eisberg and R. Resnick. *Quantum Physics of Atoms, Molecules, Solids, Nuclei and Particles*, pages 493–501. John Wiley & Sons,inc, 2 edition, 1985.

[93] R. A. Serway and Jr J. W. Jewett. *Physics for Scientists and Engineers with Modern Physics*, page 921. Brooks/Cole Cengage Learning, 9 edition, 2014.

[94] M. Gezlaff. *Fundamentals of Magnetism*, pages 72–83. Springer, 2008 edition, 2008.

[95] J. M. D. Coey. *Magnetism and Magnetic Materials*, pages 131–133. Cambrige University Press, 1st edition, 2009.

[96] K. H. J. Buschow and F. R. De Boer. *Physics of Magnetism and Magnetic Materials*, pages 34–38. Kluwer Academic Publishers, 2003.

[97] B. D. Cullity and C. D. Graham. *Introduction to Magnetic Materials*, pages 175–186. John Willey & Sons, inc., 2 edition, 2009.

[98] N. A. Spaldin. *Fundamentals of Magnetism*, pages 113–117. Cambrige University Press, 2 edition, 2011.

[99] C. Hammound. *The Basics of Crystallography and Diffraction*, pages 192–201. Oxford University Press, Inc., 3 edition, 2009.

[100] R. A. Serway, C. Vuille and J. S. Faughn. *College Physics*, pages 875–878. Brooks/Cole CEGAGE Learning, 8 edition, 2009.

[101] R. A. Serway and J. W. Jewett Jr. *Physics for Scientists and Engineers with Modern Physics*, page 997. Brooks/Cole Cengage Learning, 2014.

[102] C. Kittel. *Introduction to Solid State Physics*, page 25. John Wiley & Sons, inc., 8 edition, 2005.

[103] W. D. Callister, Jr and D. D. Rethwisch. *Materials Science and Engineering*, page 89. John Willey & Sons, Inc., 9 edition, 2014.

[104] W. D. Callister Jr and D. D. Rethwisch. *Materials Science and Engineering*, page 126. John & Sons, Inc., 9 edition, 2014.

[105] P. W. Atkins, T. L. Overton, J. P. Rourke, M. T. Weller and F. A. Armstrong. *Shriver & Atkins´ Inorganic chemistry*, page 401. Oxford University Press, 4 edition, 2010.

[106] R. A. Serway and J. W. Jewett Jr. *Physics for Scientists and Engineers with Modern Physics*, page 1252. Brooks/Cole Cengage Learning, 9 edition, 2014.

[107] D. Jiles. *Introduction to magnetism and Magnetic Materials*, page 30. Chapman and Hall, 1 edition, 1991.

[108] R. Eisberg and R. Resnick. *Quantum Physics of Atoms, Molecules, Solids, Nuclei and Particles*, page 492. 267-274. Wiley & Sons,inc, 2 edition, 1985.

[109] B. D. Cullity and C. D. Graham. *Introduction to magnetic materials*, pages 6–7. John Willey & Sons, inc., 2 edition, 2009.

[110] J. R. Kirtley, and L. Paulius and A. J. Rosenberg. *Rev. Sci. Instrum.*, 87:093702, 2016.

[111] Z. Wang, Q. Wang, H. Zhang and J. Su. *J. Supercond. Nov. Magn.*, 32:3881, 2019.

[112] O. M. Hemeda. *J. Magn. Magn. Mater.*, 251:50, 2002.

[113] N. Rani, S. Chahal, P. Kumar, R. Shukla and S. K. Singh. *J. Supercond. Nov. Magn.*, 33:1473, 2020.

[114] E. Gamello. *Electron Paramagnetic Resonance Apractioner's kit*, pages 6–7. John Willey & Sons, Inc., 1 edition, 2009.

[115] L. M. Salah, A. M. Mostafa and I. S. A. Farag. *Ceram. Int.*, 38:5605, 2012.

[116] S. Meena, L. Renuka, K. S. Anantharaju, Y. S. Vidya, H. P. Nagaswarupa, S. C. Prashantha and H. Nagabhushana. *Mater. Today: Proceedings*, 4:11773, 2017.

[117] N. Velinov, T. Petrova, I. Genova, I. Ivanov, T. Tsoncheva, V. Idakiev, B. Kunev, I. Mitov. *Mater. Res. Bul.*, 95:556, 2017.

[118] S. Yuvaraj, N. Manikandan, G. Vinitha. *Opt. Mater.*, 73:428, 2017.

[119] K. Saravanan K. Sivakumar T. K. Sakuntha S. Ambika, S. Gopinath and P. Paramasivan. *J. Supercond. Nov. Magn.*, 32:903, 2019.

[120] M. A. U. Nabi, M. Moin, M. S. Hasan, M. I. Arshad, A. Bibi, N. Amin, K. Mahmood and S. S. Ali. *J. Supercond. Nov. Magn.*, 34:1813, 2021.

[121] S. Bhaskaran, I. A. A. Omari and E. V. Gopalan. *J. Alloy. Compd.*, 884, 2021.

[122] M. Junaid, J. Jacob, M. Nadeem, M. A. Khan, S. Hayat, A. Manzoor, S. Ahmad, S. Musaddiq, W. Abbas, A. Ali, K. Mahmood and S. Hussain. *J. Supercond. Nov. Magn.*, 33:3171, 2020.

[123] P. Thakur, S. Thaneja, D. Sindhu, U. Lüders, A. Sharma, B. Ravelo and A. Thakur. *J. Supercond. Nov. Magn.*, 33:1569, 2020.

[124] M. Rezaei, S. M. Mirkazemi and S. Alamolhoda. *J. Supercond. Nov. Magn.*, 34:1397, 2021.

[125] S. Joshi and M. Kumar. *J. Supercond. Nov. Magn.*, 29:1561, 2016.

[126] I. C. Sathisha, K. Manjunatha, V. J. Angadi and R. K. Reedy. *J. Supercond. Nov. Magn.*, 33, 2020.

[127] S. Nisa, S. Atiq, S. A. Siddiqi, S. Riaz and S. Naseem. *Adv. Civil Env. Mater. Research*, 1:26, 2012.

[128] V. D. Oliveira, R. M. Rubinger, M. R. da Silva, A. F. Oliveira, G. Rodrigues and V. A. S. Ribeiro. *Mater. Res.*, 19:786, 2016.

[129] F. Majid, I. Wahid, S. Ata, I. Bibi, M. D. Ali, A. Malik, N. Alwadai, M. Iqbal and A. Nazir. *Mater. Chem. Phys.*, 264:124451, 2021.

[130] M. I. Arshad, A. Akram, K. Hussain, U. Rehman, K. Mahmood, F. Iqbal, N. Amin, S. Arshad, N. Sabir and M. A. Nabi. *J. Supercond. Nov. Magn.*, 34:589, 2021.

[131] P. Monisha, P. Priyadhashini, S. S. Gomathi and K. Pushpanathan. *J. Alloy. Compd.*, 856:157447, 2021.

[132] V. Mahdikhah, A. Atie, A. Babaei, S. Sheibani, C. W. Ow-yang and S. K. Abkenar. *J. Phys. Chem. Solids*, 134:286, 2019.

[133] E. C. Devi and I. Soibam. *J. Supercond. Nov. Magn.*, 32:1293, 2019.

[134] T. A. Nhlapo, J. Z. Msomi and T. Moyo. *J. Mol. Struct.*, 1445:131042, 2021.

[135] A. G. Roca, D. Niznansky, J. Poltierova-Vejpravova, B. Bittova, M. A. Gonzalez-Fernandez, C. J. Serna and M. P. Morales. *J. Appl. Phys.*, 105:114309, 2009.

[136] M. A. Almessiere, B. Unal, Y. Slimani, H. Gungunes, M. S. Toprak, N. Tashkandi, A. Baykal, M. Sertkol, A. V. Trukhanov, A. Yildiz, and A. Manikadan. *J. Mater. Res. Technol.*, 14:2534, 2021.

[137] B. P. Kharat, J. S. Kounsalye, M. V. Shisode and K. M. Jadhav. *J. Supercond. Nov. Magn.*, 32:341, 2019.

[138] M. Ounancer, A. Essoumhi, M. Sajieddine, A. Razouk, B. F. O. Costa, S. M. Dubiel and M. Sahlaoui. *J. Supercond. Nov. Magn.*, 33:3249, 2020.

[139] M. Shatnawi I. Bsoul A. M. Alsmadi B. Salameh G. M. Alzoubi, B. A. Albiss and G. A. Alnaẃashi. 33:3179.

[140] R. S. Melo, A. Franco Jr. and P. Banerjee. *Solid state Commun.*, 341:114560, 2022.

[141] Z. Zhang. *Mater. Today. Commun.*, 26:101734, 2021.

[142] W. B. Mdlalose, J. Z. Msomi and T. Moyo. *J. Supercond. Nov. Magn.*, 32:1821, 2019.

[143] N. Boda, K. C. B. Naidu, D. B. Basha and D. Ravinder. *J. Supercond. Nov. Magn.*, 33:1039, 2020.

[144] L. Fkhar, A. E. Kenz, M. Hamedoun, A. Benyoussef, M. A. Ali and O. Mounkachi. *J. Supercond. Nov. Magn.*, 32:381, 2021.

[145] P. A. Asogekar, S. K. Gaonkar, A. Kumar and V. M. S. Verenkar. *Mater. Res. Bull.*, 14:11330, 2021.

[146] I. Grecu, P. Samoila, P. Pascairu, C. Cojocaru, M. Ignat, I. A. Dascalu and V. Harabagiu. *Catalysts*, 13:266, 2023.

[147] M. A. Musa, D. Xu, F. Sun, H. SHao, X. Dong, R. A. Azis, A. Y. Ugya and H. A. Ari. *J. Mater. Sci.: Electron.*, 33:2375, 2020.

[148] P. A. Rao, V. Raghavendra, B. Suryanarayana, T. Paulos, N. Murali, P.V.S.K.P. Varma, R. G. Prasad, Y. Ramakrishna and K. Chandramouli. *Res. Phys.*, 19:103487, 2020.

[149] M. Shakil, U. Inayat, N. R. Khalid, M. Tanveer, S. S. A. Gillani, H. Tarriq, A. Shah, A. Mahmood and A. Dahshan. *J. Phys. Chem. Solids*, 161:110419, 2022.

[150] H. Ghorbani, M. Eshraghi and A. A. S. Dodaran. *Phys. B: Condens. Matter*, 634:413816, 2022.

[151] M. K. Bharti, S. Chalia, P. Thakur and A. Thakur. *J. Supercond. Nov. Magn.*, 34:2591, 2021.

[152] M. M. N. Ansari, S.Khan, and N. Ahmad. *J. Mater. Sci.:Mater. Electron.*, 30:17630, 2019.

[153] S. A. V. Prasad, M. Deepty, P. N. Ramesh, G. Prasad, K. Srinivasaro, C. Srinivas, K. V. Babu, E. R. Kumar, N. K. Mohan and D. L. Sastry. *Ceram. Int.*, 44:10517, 2018.

[154] M. Irfan, N. Dogan, A. Bingolbali and F. Aliew. *J. Magn. Magn. Mater.*, 537:16850, 2021.

[155] M. Saini, R. Shukla, S. K. Singh. *Mater. Sci. Mater. Electr.*, 29:2044, 2019.

[156] J. B. M. Cunha P. A. M. Vitor, J. Venturini and C. P. Bergmann. *J. Alloy. Compd.*, 851:156799.

[157] A. Hai, B. Alqassem, G. Bharath, K. Rambabu, I. Othman, M. A. Haija and F. Banat. *Electrochim. Acta*, 363:137083, 2020.

[158] S. Das, C. Manoharan, M. Venkateshwarlu, P. Dhamodharan. *Mater. Sci. Mater. Electr.*, 30:19880, 2019.

[159] C. C. Naik and A. V. Salker. *J. Supercond. Nov. Magn.*, 32:3655, 2019.

[160] M. Amir, H. Gungunes, Y. Slimani, N. Tashkhandi, H. S. E. Sayed, F. Aldakheel, M. Sertkol, H. Sozeri, A. Manikandan, I. Ercan and A. Baykal. *J. Supercond. Nov. Magn.*, 32:557.

[161] A. Kumar, N. Yadav, D. S. Rana, P. Kumar, M. Arora and R. P. Pant. *J. Magn. Magn. Mater.*, 394:379, 2015.

[162] S. Kumari, M. K. Manglam, A. Shukla, L. Kumar, P. Seal, J. P. Borah and M. Kar. *Phys. B: Condens. Matter*, 621:413280, 2021.

[163] A. B. Andrade, N. S. Ferreira, M. E. G. Valerio. *RSC Adv.*, 7:26839, 2017.

[164] J. M. Massoudi, K. Smari, E. Nouri, K. Dhahri, S. Khirouni, Bertaina, L. Bessais and A. K. Hlil. *RSC. Adv.*, 10:34556, 2020.

[165] M. Khairy, W. A. Bayoumy,S. S. Selima and M. A. Mousa. *J. Mater.Res.*, 35:2652, 2020.